ABSTRACT

Adaptive Load Impedance Optimization for Power Amplifiers in Reconfigurable Radar Transmitters

Joshua Lee Martin, M.S.E.C.E

Mentor: Charles Passant Baylis II, Ph.D.

A fundamental tradeoff exists in radar transmitter design between linearity and efficiency due to the signal amplification. These transmitters are driven into saturation in order to increase efficiency, but may potentially violate regulatory spectral mask limitations. An adaptive method for optimizing linearity and efficiency for power amplifiers in radar transmitters is presented. This approach uses intelligent search techniques with load-pull measurements for power-added efficiency (PAE) and adjacent channel power ratio (ACPR) to dynamically maximize the PAE while meeting spectral requirements. Using load-tuning, an algorithm performs a steepest ascent search for the PAE optimum load reflection coefficient, followed by a steepest descent search for ACPR. The steepest descent search, when begun at the PAE optimum, approximates the Pareto optimal frontier between the two objectives. This trace enables PAE to be maximized for an imposed limit on ACPR, optimizing the performance of adaptive radar transmitters under spectral mask constraints.

Adaptive Load Impedance Optimization for Power Amplifiers in Reconfigurable Radar Transmitters

by

Joshua Lee Martin

A Thesis

Approved by the Department of Electrical and Computer Engineering

_____

Kwang Lee, Ph.D., Chairperson

Submitted to the Graduate Faculty of
Baylor University in Partial Fulfillment of the
Requirements for the Degree
of

Master of Science

Approved by the Thesis Committee

_____

Charles Baylis, Ph.D., Chairperson

_____

Robert Marks, Ph.D.

_____

David J. Ryden, Ph.D.

Accepted by the Graduate School

December 2012

_____

J. Larry Lyon, Ph.D., Dean

Page bearing signatures is kept on file in the Graduate School.

TABLE OF CONTENTS

LIST OF FIGURES

LIST OF TABLES

ACKNOWLEDGEMENTS

I would like to thank my thesis advisor, Dr. Charles Baylis, who has provided excellent guidance, encouragement, progressive comments, and sufficient funding for this work. Dr. Robert Marks has contributed a great deal to the development of this work through mathematical insights and ideas. He has dedicated time over and above what is expected of a committee member in developing my understanding of Pareto optimization. David Ryden has also devoted his time through editing and ensuring the ideas of this document are well communicated. I would like to acknowledge Agilent Technologies for a cost-free loan of the Advanced Design System Software, Modelithics for the donation of simulation model libraries, and Maury Microwave for the donation of SNP customization files. Graduate students Matthew Moldovan, Loria Wang, David Moon, Robert Scott, Obi Akinbule, and Brandon Herrera have provided invaluable assistance in calibrating equipment for and performing load-pull measurements. I would also like to acknowledge our sponsors Lawrence Cohen and Eric Mokole from the Naval Research Laboratory. Their guidance and expertise in radar systems has been invaluable in the continuation of this work. Furthermore, I would like to express my gratitude to Naval Research Laboratories for providing the funding and opportunity for this work.

Finally I would like to thank to my wife, Brittney Martin, for love and support throughout the completion of this work. My parents, David and Lori Martin, have provided wise council throughout my pursuits at Baylor. Earl and Pasty Taylor, and the late Jewel Baughman, have also been greatly instrumental in encouraging and supporting my efforts.

CHAPTER ONE

Introduction

The concept of reconfigurable or adaptive radar is a system which, in addition to traditional detection purposes, possesses the ability to adapt its emissions to accommodate diverse operating environments. These types of radar systems are often capable of producing unique emissions for improving target detection [1, 2, 3], operating in multiple frequency bands [4], and adjusting to various spectrum obstacles [5]. Information pertaining to the radar's operating environment is incorporated through various sources, such as an environmental dynamic database [6]. The use of this information enables the reconfigurable radar to fulfill missions in which accurate real time sensing is paramount.

Emissions from radar transmitters are affected by factors such as signal choice and constituent circuitry. Influences for selecting the proper waveform include minimizing the ambiguity function [7], sidelobe suppression [8], and increasing signal to noise ratio at the receiver [2]. Additionally, the amplification stage of the radar transmitter introduces many unwanted spurious emissions at high output powers [9]. These spectral effects degrade the system linearity and produce electromagnetic interference separate from the intended emissions.

The spurious emissions from high power radar transmitters possess the ability to interfere with neighboring communication channels [10]. Communication systems typically operate at power levels much lower than radar systems and are sensitive to signal distortion. Unwanted interference from radar systems may cause bit errors and

reduced signal to noise ratio. Radar systems operate in a broad range of the electromagnetic spectrum and thus have the potential to affect a large number of neighboring communication channels. The United States has assigned the FCC with the responsibility allocating certain frequencies for which commercial electromagnetic emissions may operate. Government frequency spectrum is regulated separately by the NTIA, which includes radar emissions. The separation of different emissions is accomplished by imposing strict operating limitations on users of a particular band, such as maximum operating power, transmit time, and emission bandwidth. These restrictions ensure both separation among the various frequency channels and that multiple users can coexist within the same bandwidth.

Radar system emissions in particular are regulated by the RSEC criteria [11]. The restrictions imposed on the transmitted waveforms are implemented in the form of a spectral mask, a tool which profiles the relative power between in-band and out-of-band channels for an allocated radar frequency band. This regulation specifically targets out of band characteristics of the emitted spectrum and ensures that any undesired signals outside the intended bandwidth are sufficiently attenuated. High power radar systems which emit significant spectral leakage may face significant performance degradations from reduced output power should the spectral constraints become increasingly strict. The immediate consequence of reduced output power for radar systems is maximum detectable range, but also could severely hinder the operating efficiency of the amplification stage. The latter issue is significant from an energy conservation perspective since less of the large power required for amplification is used to amplify the signal and instead contributes to undesired factors such as temperature increase. Recent developments in economically-driven wireless applications are threatening to intensify

the regulations on radar emissions. As of 2010, the National Broadband Plan mandates the release of 500 MHz of additional electromagnetic spectrum to be used for the emerging wireless broadband networks [12]. Consequentially, radar systems which operate in this frequency range will be further limited in performance due to stricter spectral mask requirements.

Ensuring the effectiveness of radar system performance is critical for both commercial and military applications. As wireless technologies and applications continue to advance, radar emissions must adapt to an ever-changing spectrum configuration and utilize all available detection capabilities under spectral mask constraints. Characterizing radar circuitry in order to minimize out-of band emissions has been achieved through load-pull characterization, along with other metrics such as output power, efficiency, etc. Additionally, radar systems may need to operate in a dynamic spectrum access environment in which emissions must share the same bandwidth. This development would require radar systems to be cooperative with other types of emissions.

Adaptive load tuning networks can provide a method for tuning amplification circuitry to mitigate spurious emissions at high power operation. Chapter 2 analyzes how nonlinear amplifier operation influences transmitter emissions and device efficiency, as well as design techniques for accommodating the tradeoff between linearity and efficiency. Another method for designing a tradeoff between linearity and efficiency is to examine the Pareto optimal curve between PAE and ACPR. Chapter 3 explores a method for generating Pareto optimization curves for PAE and ACPR in designing matching networks with load-pull. This technique parameterizes two objective functions, and forms a combined set which contains the solution for a particular importance weight.

The Pareto optimization curve allows for the efficiency to be maximized given a fixed spectral constraint. The application of the Pareto curve between PAE and ACPR serves as an a priori technique to amplifier matching network design using load-pull measurements.

Although the Pareto curve generated between PAE and ACPR provides a useful a priori tool for amplifier matching network design, reconfigurable transmitters must be able to adapt in real time to changing spectral constraints, modulated excitations, and device thermal effects. Chapter 4 proposes a method for estimating the Pareto curve in real-time using a sequential peak search method. Generating this tradeoff path utilizes a sequential search for both objective discovery and Pareto tracing.

Chapter 5 shows how this method is implemented using both software and reconfigurable load-pull test benches. The test benches are capable of producing arbitrary radar waveforms for exciting the DUT, as well as performing simultaneous PAE and ACPR measurements. The measurement test bench in particular is orchestrated by a central PC and executes the algorithm in Chapter 4.

The results of the steepest ascent search for multiple initializations are shown in Chapter 6. Various settings for steepest ascent are shown to have a dramatic effect on the number of measurements required for generating the Pareto curve. The effectiveness of the algorithm is determined by the consistent convergence point for each initial starting point, as well as the approximated magnitudes for PAE and ACPR.

Performing an adaptive load-pull for bi-objective optimization can be useful for reconfigurable radar systems operating in different environments and for various waveforms. Chapter 7 explains how impedance tuning can further extend the capabilities of radar transmitter performance under different modulation schemes in a dynamic

spectrum environment. Possible improvements upon the current algorithm are also discussed which could reduce the algorithm measurement time.

The goal of this work is to provide a method for applying circuit optimization techniques to maximize radar performance under spectral constraints. The broader impact of this work provides a foundation for future adaptive solutions which allow for hardware level reconfiguration in the field. Due to the application of digital modulation techniques to adaptive radar, impedance tuning using load-pull enables optimization of amplifier circuitry to fulfill certain system requirements for arbitrary signal excitations.

CHAPTER TWO

Nonlinear Amplifier Effects and Measurements

Amplifier behaviors vary dramatically depending upon the input signal used for excitation. A simple way to model such behaviors is through small signal excitation using S-parameters. This model, however, is only valid in cases where the amplifier transfer function is approximately linear. Once the amplifier is pushed near saturation, which is common in radar transmitter applications, the transfer function becomes increasingly nonlinear. These significant changes in the amplifier transfer function lead to unwanted effects, such as intermodulation distortion. Intermodulation distortion occurs for modulated signals under large signal conditions which produce interfering tones inside and outside of the emission bandwidth. Although these distortions are undesired, high power and efficient amplifier operation can only be accomplished in amplifier saturation. Nonlinear amplifier behavior can be characterized using load-pull techniques. This method provides an empirical study of the amplifier for a given nonlinear operating condition. This chapter explains the theory behind using load-pull for designing RF amplifiers and emphasizes the use of ACPR for quantifying the system linearity.

2.1 Intermodulation Distortion

The production of out-of-band signals by the amplifier is due to the nonlinear transfer characteristics under large signal conditions. The degree of the nonlinearity is dependent upon the magnitude of the input waveform. Intermodulation distortion does not occur for CW signals, where only a single tone is present. Most RF systems,

however, use modulated signals due to increased information capacity. In signals with multiple tones in close proximity, or broadband signals, additional nearby frequency content is produced from intermodulation of frequency components in the desired signal. A simple and well known measure of intermodulation distortion is demonstrated through a two tone excitation [13, 14]. Assuming a weak nonlinear system, the intermodulation products may be approximated using the power series. Consider the amplifier output, v_o, as the summation of an infinite number of nonlinear products, v_i:

$$v_o = \sum_{n=0}^{\infty} a_n v_i^{\,n} \tag{1}$$

where a_n are coefficients weights. The two tone excitation is the input in this case and is represented by:

$$v_i = A\cos\omega_1 t + B\cos\omega_2 t \tag{2}$$

$$v_o = \sum_{n=0}^{\infty} a_n \left(A\cos\omega_1 t + B\cos\omega_2 t\right)^n \tag{3}$$

Deriving the amplifier output for three terms yields

$$\begin{aligned} v_o = a_0 + a_1\left(A\cos\omega_1 t + B\cos\omega_2 t\right) + a_2\left(A\cos\omega_1 t + B\cos\omega_2 t\right)^2 \\ + a_3\left(A\cos\omega_1 t + B\cos\omega_2 t\right)^3 \end{aligned} \tag{4}$$

$$\begin{aligned} v_o = a_0 + a_1\left(A\cos\omega_1 t + B\cos\omega_2 t\right) \\ + a_2\left(A^2\cos(\omega_1 t)^2 + B^2\cos(\omega_2 t)^2 + 2AB\cos(\omega_1 t)\cos(\omega_2 t)\right) \\ + a_3\left(A^3\cos(\omega_1 t)^3 + B^3\cos(\omega_2 t)^3 + A^2 B\cos(\omega_1 t)^2\cos(\omega_2 t)\right. \\ \left. + AB^2\cos(\omega_1 t)\cos(\omega_2 t)^2\right) \end{aligned} \tag{5}$$

$$
\begin{aligned}
v_o = a_0 + a_1(A\cos\omega_1 t + B\cos\omega_2 t) + a_2(A^2\cos(\omega_1 t)^2 + B^2\cos(\omega_2 t)^2 \\
+ AB(\cos(\omega_1 t + \omega_2 t) + \cos(\omega_1 t - \omega_2 t))) + a_3(A^3\cos(\omega_1 t)^3 + B^3\cos(\omega_2 t)^3 \\
+ \frac{A^2 B}{2}(\cos(\omega_2 t) + \cos(2\omega_1 t + \omega_2 t) + \cos(2\omega_1 t - \omega_2 t)) \\
+ \frac{AB^2}{2}(\cos(\omega_1 t) + \cos(2\omega_2 t + \omega_1 t) + \cos(2\omega_2 t - \omega_1 t)))
\end{aligned}
\tag{6}
$$

The two tone intermodulation spectrum is shown in Figure 2.1. Third-order intermodulation in (6) include components at $2\omega_1 + \omega_2$ and $2\omega_2 + \omega_1$ and contributes significantly to the amount of distortion produced from large signal excitation [15]. The power series model for intermodulation may be used for weak nonlinear operation at power levels below the amplifier 1dB compression point according to Cripps [14]. Amplifier compression relates deviation of nonlinear gain from linear gain for operation near saturation. Higher order terms should be considered for the case of power amplifiers beyond 1dB compression, and can dominate lower-order effects.

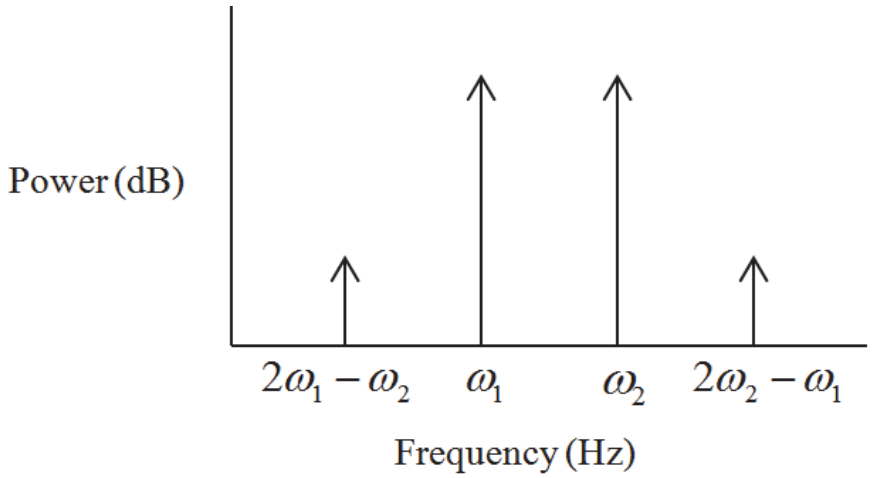

Figure 2.1: Two-Tone Frequency Spectrum for Weak Nonlinearity

Moreover, Cripps indicates that amplifiers driven to greater levels of compression can no longer be modeled using a weak nonlinearity, but rather must be assessed as a

strong nonlinearity. This strong nonlinearity is representative of an amplifier's inability to increase the output signal amplitude for corresponding increases in input signal amplitude. Additionally, strong nonlinearities introduce AM-PM effects. These added effects represent a change in the phase characteristic of the amplifier as the input power becomes increasingly large. The two-tone test has inherent limitations when applied to radar systems considering that many transmitters operate at or near saturation [16], and utilize a variety of modulated waveforms [17]. A more useful way to evaluate amplifier linearity relating to spurious emissions is to compare the measured output power in the assigned channel of operation and adjacent channels. The adjacent-channel power ratio (ACPR) quantifies this relationship by taking a ratio between the power in the main signal bandwidth and an adjacent bandwidth offset from the nominal operating frequency [18, 19, 20].

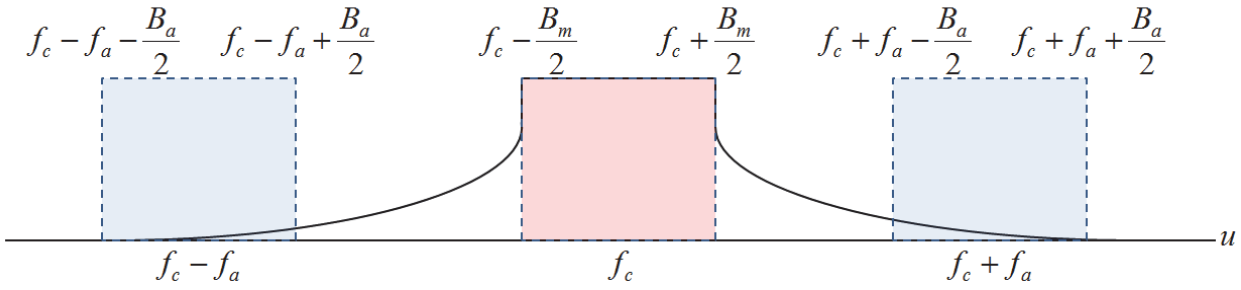

Figure 2.2: Modulated Signal Spectrum with Main (red) and Adjacent (blue) Channel Bandwidths

The ACPR channels are shown for an arbitrary modulated frequency spectrum in Figure 2.2, where f_c is the carrier frequency, f_a is the adjacent channel offset, B_m is the main channel bandwidth, and B_a is the adjacent channel bandwidth. The waveform spreading is shown to fall in the vicinity of the adjacent channel, which can possibly interfere with other emissions operating within the adjacent channel bandwidth. The

power in each channel is quantified by integrating the power of the individual tones over the associated bandwidth. Assuming the modulated signal frequency spectrum in Figure 2.2 is symmetric, the upper and lower ACPR, P_{ACPR} , is mathematically expressed as a ratio of the total power of either adjacent channel channel P_A to the main channel P_m is given by (7).

$$P_{ACPR} = \frac{P_A}{p_m} \tag{7}$$

Using ACPR, the spurious emissions from all nonlinear terms in (1) are accounted for in a single integration bandwidth. Comparing the integration bandwidth of the main channel allows for the distortion level to be evaluated, where higher values indicate increased distortion and vice versa [20]. ACPR is a measure of system linearity, though there other ways to quantify this attribute. Error vector magnitude (EVM) is often used to quantify the in-band distortions that occur from nonlinear amplifier operation, and is used by Jonggyun to measure the RF path imbalances of a LINC amplifier configuration [21].

2.2 Efficiency and Tradeoff with Linearity

Another key factor associated with amplifier nonlinearity is a boost in efficiency. Efficiency in amplifier design measures how well an amplifier converts DC power to AC power, which is used to amplify the device. Specifically, power-added efficiency (PAE) is commonly used to quantify this performance factor and is given by (8).

$$PAE = \frac{P_o - P_i}{P_{DC}} \tag{8}$$

P_o is the total amplifier output power in watts, P_i is the total amplifier input power in watts, and P_{DC} is the total DC power. PAE is expressed in terms of percentage of DC

power which is converted to AC power. An increase in efficiency is often desired for reduced carbon emissions, maximizing battery life in mobile applications, achieving high power output, and reducing cooling requirements for transmitter base stations [22].

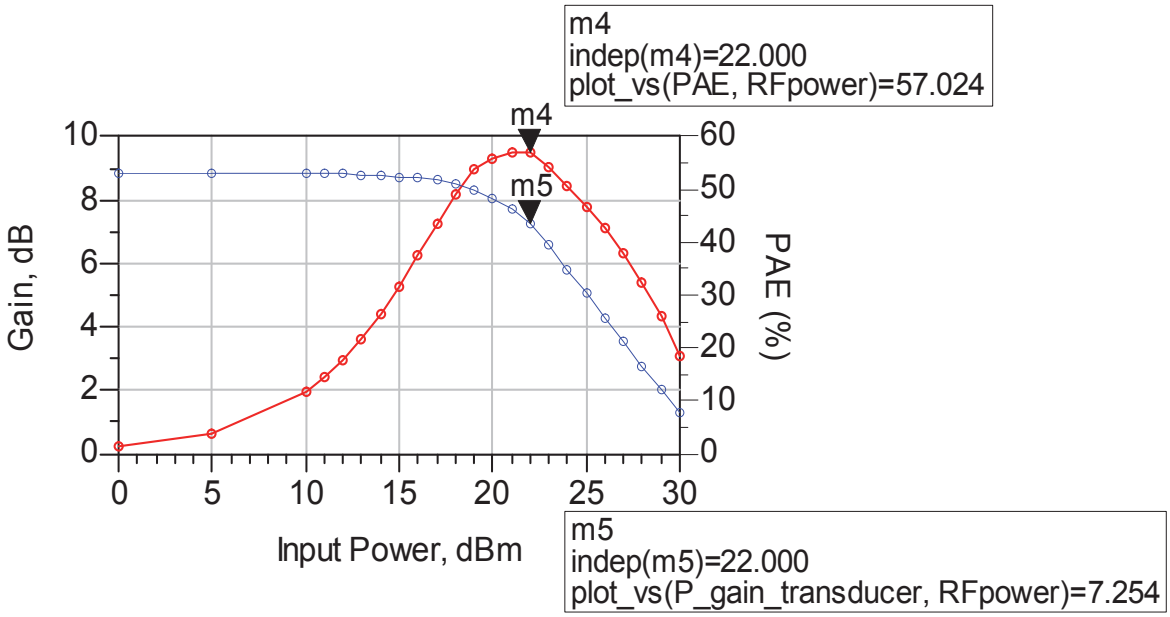

Figure 2.3: Gain (blue) and PAE (red) for GaAs MESFET Power Sweep Reprinted from [28]

High efficiency, however, is achieved from amplifier devices operating near saturation. Operating the amplifier near saturation causes unwanted signal distortions as described in the previous section. As such, linearity versus efficiency is a fundamental tradeoff of power-amplifier design. This is based on the fact that high device efficiency is achieved through saturation, which also introduces substantial intermodulation. Figure 2.3 illustrates this tradeoff for a simulated power sweep for a GaAs MESFET amplifier. The amplifier is swept over a range of input power values. The gain curve is constant for low input power values, displaying linear performance, but becomes increasingly reduced for higher output powers, demonstrating nonlinear behavior.

The degree of the nonlinearity relates directly to the amount of distortion and spectral spreading experienced by the output emission. There are several techniques for overcoming the tradeoff between linearity and efficiency. There has been interest in optimizing both linearity and efficiency using load-pull for Doherty amplifiers [23, 24, 25], as well as reducing intermodulation distortion in radar and communications systems [18, 26, 27, 28, 29]. Methods for optimizing linearity and efficiency have been shown by techniques such as dynamic bias [30, 31], envelope following [32, 33], and envelope tracking [34, 35]. These methods, however, fundamentally limit the maximum efficiency achievable due to linear amplifier operation [36]. Another technique for improving both linearity and efficiency is through the use of the linear amplification with nonlinear components (LINC) approach, which separates the input signals into two out-of-phase components and recombines them after separate amplification [21, 37]. This method, however, losses efficiency in the combiner stage and also suffers from bandwidth, complexity, and linearity issues [18, 36]. One of the most influential factors that influences amplifier linearity and efficiency is the choice of matching impedances.

2.3 Amplifier Characterization with Load-Pull

A common characterization method used to identify the effects of matching impedance on performance is load-pull measurements [38]. Load-pull is an empirical technique for analyzing an amplifier output metric as a function of impedance [14]. One of the reasons this measurement is such a powerful tool is that it enables models to be extracted for amplifiers near saturation. These measurements share a trait with linear S-parameter analysis in that contours can be mapped onto the Smith Chart for various performance criteria.

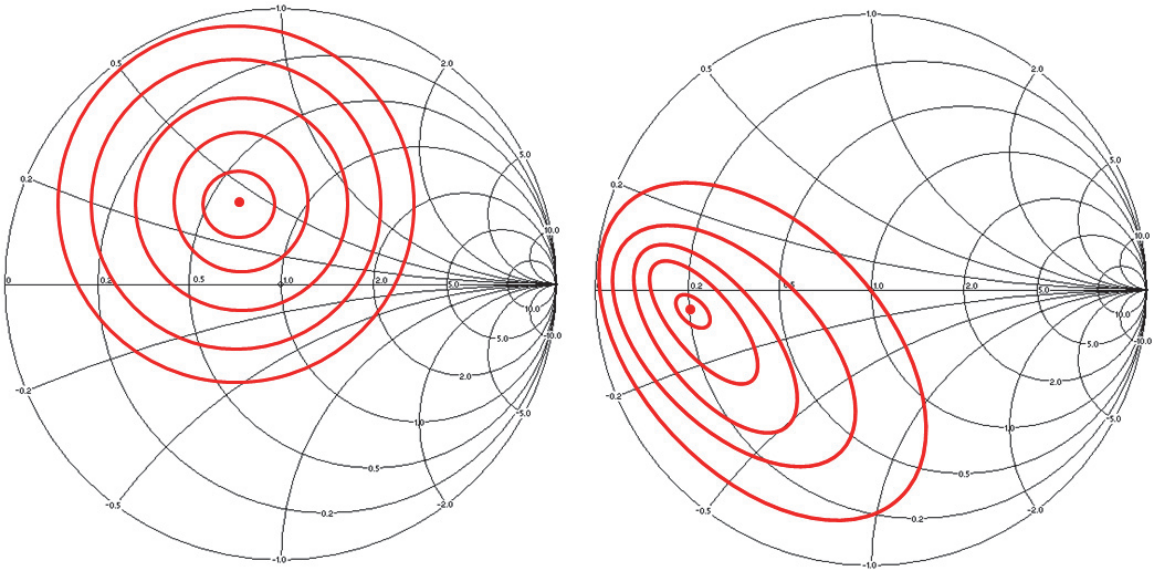

(a) (b)

Figure 2.4: Generic Contours for (a) Small and (b) Large Signal Amplifier Excitation

These contours represent curves of constant magnitude for which the magnitude of a measured attribute is constant. The set of all contours for a particular dataset forms a contour map imposed onto the Smith Chart. Figure 2.4a shows typical contours for an arbitrary dataset evaluated using small signal S-parameters. These contours form circles around a central optimum point.

As the amplifier approaches nonlinear operation, however, the contours can become ovals rather than circles as shown in Figure 2.4b. Additionally, the optimum load reflection coefficient for a particular characteristic can drift as the device becomes more nonlinear. Although load-pull techniques vary depending on the application, the measurement setup typically consists of an excitation source, a tunable impedance network, and a power sensor [14]. Figure 2.5 shows a diagram of this basic setup for a measurement of output power.

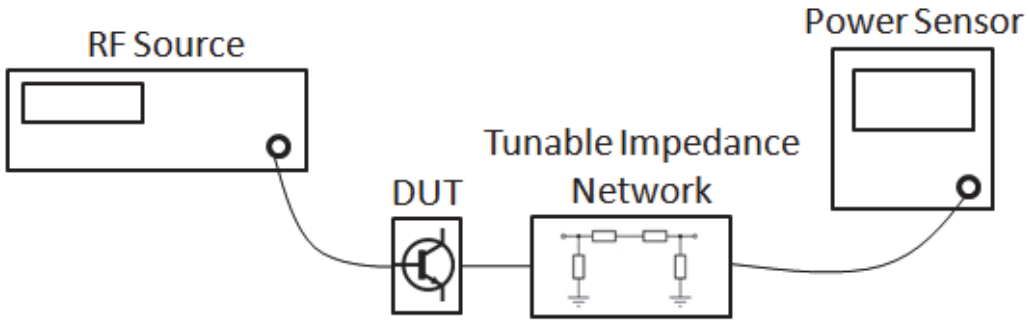

Figure 2.5: Basic Load-Pull Setup for Measuring Output Power

Characterizing the DUT consists of varying the impedance tuner over a relevant set of load reflection coefficients and recording the output power at each location. The output power measured can be used to calculate other qualitative factors such as gain, PAE, etc. Additionally, ACPR load-pull may be performed to quantify the amplifier linearity. This requires an additional tool, a spectrum analyzer, to measure the power at individual frequencies. This basic setup is referred to as fundamental load pull, since only the fundamental harmonic is measured. There are many cases in which harmonic load pull is necessary to design for harmonic matching [14, 39, 40]. This matching technique can be used to significantly increase device efficiency using second and third harmonic matching [41]. Active load-pull is another method used for modeling RF systems. This measurement includes an active device as part of the impedance tuning apparatus. The active element is necessary in order to compensate for losses in the measurement and provide a larger available VSWR [14].

2.4 Conclusion

Characterizing RF amplifiers is essential to ensuring that the overall system is able to meet conflicting constraints such as PAE and ACPR. Radar systems require knowledge pertaining to amplifier nonlinearities in order to ensure spectral conformity.

Such systems can be designed using the results of load-pull measurements, which provide description of amplifier traits as a function of impedance. Although these methods provide an empirical study of linearity and efficiency tradeoff for amplifier design, the question remains on how a decision is reached as to which candidate impedance is selected. The next chapter discusses intelligent algorithms which can be used to design for specific performance criteria.

CHAPTER THREE

Pareto Tradeoff Analysis for Load-Pull Contours

Designing amplifier matching networks for multiple objective criteria often results in performance tradeoffs. These tradeoffs occur when the optima of two objectives cannot be reached simultaneously using individual matching impedances. Because minimization of spectral spreading is important in radar systems, this thesis discusses the Pareto optimization for the fundamentally conflicting criteria of linearity and efficiency in radar power amplifiers. Although there are several methods for optimizing for linearity and efficiency in power amplifier design, the choice of output matching network is among the greatest of deciding factors. Additionally, achieving high device efficiency often requires the amplifier to be driven near saturation; unfortunately, significant spectral spreading occurs from the resultant nonlinearity of the amplifier. Load-pull has been shown to be an effective means of empirically modeling nonlinear amplifiers for matching network design. Despite the widespread use of load-pull measurements, the process of selecting an optimal tradeoff between conflicting objectives remains highly subjective in amplifier design and load pull. Bi-objective Pareto optimization is proposed in this chapter as a method for mapping a tradeoff line between linearity and efficiency using load-pull techniques. The Pareto curve, mapped to the Smith Chart, provides the optimal tradeoff between linearity and efficiency depending on the relative importance of these two objectives. This curve too also serves as a design reference for negotiating the tradeoff between conflicting criteria in amplifier matching network design.

3.1 Pareto Optimization for Fuzzy Convex Contours

Load-pull has been shown in the previous section to map contours onto the complex impedance plane for a particular amplifier characteristic. The load-pull contours describe the magnitude trend of a particular objective as a function of load impedance. The contours produced for small signal amplifier operation are circular and can be predicted by the S-parameters [41]. These assumptions become invalid, however, once the amplifier reaches nonlinear operation. Load-pull contours for output power tend to deviate from a circular to an ovular shape, and become skewed as the degree of amplifier nonlinearity increases [42, 43, 44]. Extending these assumptions to the objective functions of PAE and ACPR, it becomes important to classify the functions which the contours specify. The types of objective functions being considered are fuzzy convex sets as shown in Figure 3.1. These functions encompass a wide range of unimodal objectives which the contours which are shown in Chapter 2, including those for PAE and ACPR. A one dimensional example will be shown to demonstrate the derivation of Pareto optimal solutions, and will be extended to two dimensions for application to load-pull. Figure 3.1 shows a magnitude plot of an arbitrary, fuzzy convex objective function $p(x)$, where $x \in X$. The definition of fuzzy convex sets follows from Zadeh [45] in (1).

$$p\left[\lambda x_1 + (1-\lambda)x_2\right] \geq \min\left[p(x_1), p(x_2)\right] \tag{1}$$

$$\{\lambda \in \Re \mid 0 \leq \lambda \leq 1\}$$

This definition of convexity does not require that the function $p(X)$ be a convex function of X, and therefore includes sets which are both strictly convex as well as quasi-convex [46, 47]. The points x_1 and x_2 represent locations with magnitudes p_1 and p_2 on the

boundary of $p(x)$. The expression in (1) explains that the continuum of magnitudes between p_1 and p_2 must be greater than or equal to the minimum magnitude of either point. These magnitudes are expressed in terms of a convex combination weighting in the left portion of (1), which must be true inside of the set. Defining convexity in this way is required in order to define the Pareto optimization, or optimal tradeoff, between multiple objectives such as PAE and ACPR.

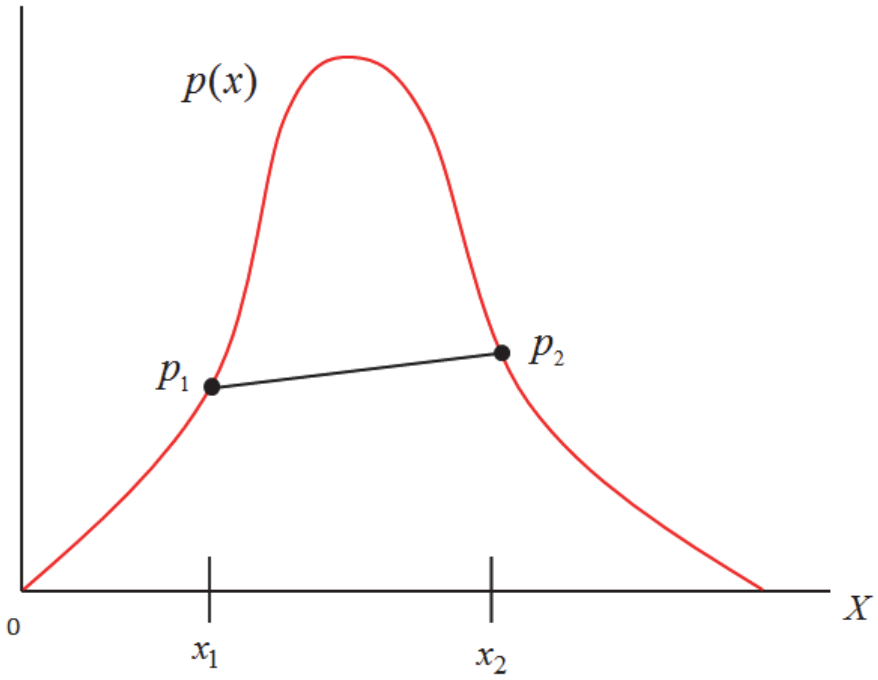

Figure 3.1: Fuzzy Convex for Objective Function $p(x)$ (red)

The Pareto optimization is used in design scenarios where a tradeoff must be made between two desired objectives [48, 49]. Each of the objectives is dependent on a common variable which influences their individual outcome. The Pareto solutions correspond to those variable states which result in a weighted tradeoff between the two objectives. Computing this weighting requires an examination of the definition of Pareto

optimum. Consider two fuzzy convex objective functions, $p(x)$ and $a(x)$, where the Pareto optimization over X is defined as

$$\begin{aligned} p_o &= \max\big(p(x)\big) \\ s.t. \quad & a(x) \geq a_o . \end{aligned} \tag{2}$$

Figure 3.2 shows the magnitude constraint a_o on $a(x)$ and solution p_o on $p(x)$. The magnitude p_o is the maximum value on $p(x)$ given the constraint a_o on $a(x)$, and $p(x_B) = p_o$ is a Pareto optimal point by the definition on (1).

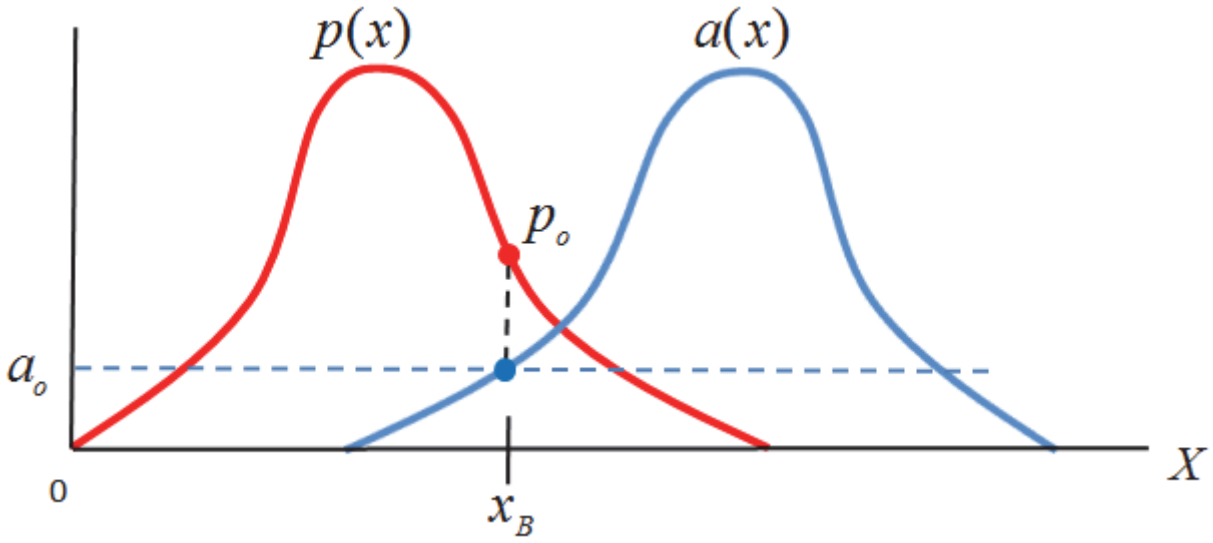

Figure 3.2: Maximizing $p(x)$ for a Constraint a_o on $a(x)$

Theorem 1: Let x_p and x_a be the maximum magnitudes of $p(x)$ and $a(x)$ respectively. For every magnitude a_o of on $a(x)$ on the closed interval $[x_p, x_a]$, there exists a p_o on the boundary of $p(x)$ which is a Pareto optimal solution.

Considers that the function $p(x)$, for a given constraint a_o, is always maximized along the boundary. These boundary points can be defined in terms of the level sets $L_c(p)$ and $L_c(a)$ in (3) and (4).

$$L_c(p) = \{x \in X \mid p(x) = p_o\} \tag{3}$$

$$L_c(a) = \{x \in X \mid a(x) = a_o\} \tag{4}$$

An extension of Theorem 1 is that for every level set $L_c(a_o)$, there exists a $L_c(p_o)$ which satisfies the Pareto solution at the boundary point x_B of both level sets. A Pareto optimal point also exists at the points where the contours of the level sets are tangent [50], which is most obvious at the cusp between the two functions. Figure 3.3 shows the cusp formed by the intersection of the two sets $p(x)$ and $a(x)$, where the two levels sets $L_c(p_o)$ and $L_c(a_o)$, intersect at the point x_B.

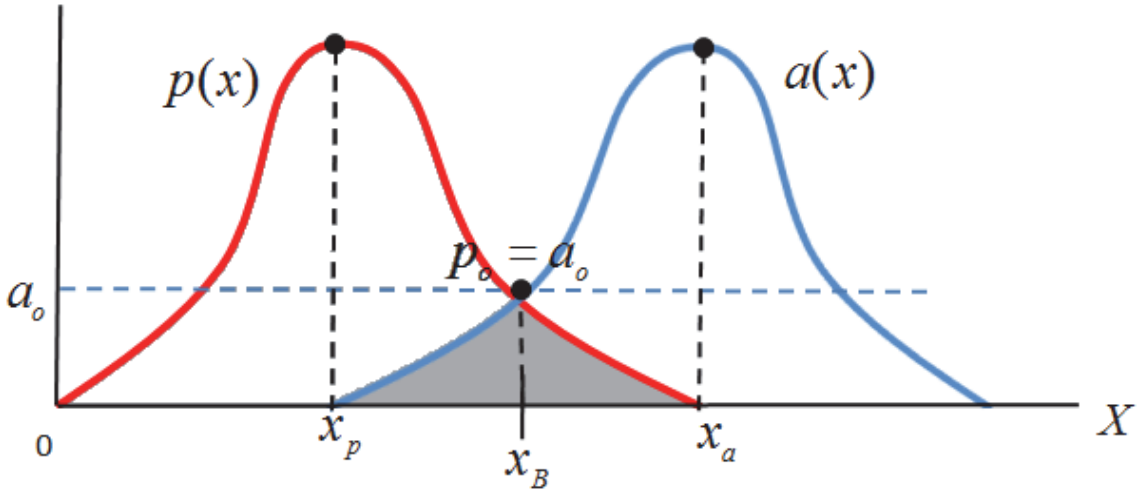

Figure 3.3: Level Sets at the Cusp (gray) of $p(x)$ (red) and $a(x)$

The tip of the cusp represents a Pareto point for which $p_o = a_o$ and can be defined as the maximum of the intersection between $p(x)$ and $a(x)$ in (5), which in fuzzy set theory [45] is also the maximum of the minimum of the two functions.

$$\max(p(x) \cap a(x)) = \max(\min(p(x), a(x))) \tag{5}$$

The cusp is unique for strongly convex functions [45], and thus gives a unique Pareto solution at the point x_B between the two functions. Using (5), the point x_B can be evaluated by evaluating the argument at the cusp in (6).

$$x_B = \arg\left(\max\left(\min\left(p(x), a(x)\right)\right)\right) \tag{6}$$

The cusp has been carefully described in order to explain how it can be used to evaluate the entire Pareto curve between $p(x)$ and $a(x)$. Consider the example in Figure 3.2 which shows the Pareto optimum p_o on $p(x)$ for a fixed a_o on $a(x)$, and $p_o \neq a_o$ at the Pareto location x_B. A cusp can be defined on the interval $[x_p, x_a]$ where the magnitude of the two functions are equal, so let there be a constant $\beta > 0$ such that

$$\beta p(x_B) = a(x_B). \tag{7}$$

The constant β is a value which causes the value of the two functions at x_B to be equal, and also forms a cusp between the two functions at x_B. The location of the cusp modifies (6) to

$$x_B = \arg\left(\max\left(\min\left(\beta p(x), a(x)\right)\right)\right). \tag{8}$$

The movement of the cusp along the interval $[x_p, x_a]$ traces the Pareto front for two reasons. As stated previously, the cusp occurs at the point at which the magnitudes of the two objectives are equal. Moreover, the level curves which correspond to the magnitudes of the two functions intersect at the tip of the cusp, which is by definition a Pareto solution. The second reason is that for strictly increasing functions $f(\cdot)$, the level curves of $p(x)$ are the same as the contours of $f(p(x, y))$; that is, a strictly increasing function is order-preserving. The values assigned to each level set changes, but the level curve shape does not. A definition of an order-preserving transformation [51] would be

the following: let $p: X \to \mathbb{R}$ be a real valued function on the set X. The function $\tilde{p}: X \to \mathbb{R}$ is an order preserving transformation of p if there is a strictly increasing real function $f: p(x) \to \mathbb{R}$ such that for every $x \in X, \tilde{p}(x) = f(p(x))$. Every location at which the cusp is located on X for a given β will be Pareto optimal by definition. The movement of the cusp, therefore, traces unique Pareto solution since the level curves remain in the same locations on X under multiplication, where the location of a particular Pareto point for a given β is shown by (8). The constant β can be parameterized such that

$$\beta = \frac{\alpha}{1-\alpha}. \tag{9}$$

The parameterization by α is necessary to meaningfully adjust the two objective functions in a meaningful fashion. This parameterization modifies (8) to be

$$x_B = \arg\left(\max\left(\min\left(\alpha p(x), (1-\alpha)a(x)\right)\right)\right) \tag{10}$$

$$0 \le \alpha \le 1 \quad .$$

The Pareto optimization is based on a fix-one, maximize the other approach. The use of α in (10) allows for the two objectives to be weighted proportionally according to the importance, which is from least important to most important for α between zero and one. The parameterization by α preserves the features of the cusp and still allows the locations of the Pareto optimal points to be located. This technique for tracing the Pareto front for a simple function will now be extended to the load-pull contours.

Applying these Pareto solutions to load-pull contours requires that the functions be extended to functions of two dimensional variables. Consider the level curves shown in Figure 3.4 for functions $p(\vec{x})$ and $a(\vec{x})$, where $\vec{x} = \begin{bmatrix} x \\ y \end{bmatrix}$ and $x, y \in X$. The case of setting a magnitude limit for one objective and maximizing the other as in (1) applies to

the convex level sets formed by fuzzy convex objective functions $p(\vec{x})$ and $a(\vec{x})$. The point (x_B, y_B) is a solution on the Pareto front for a fixed a_o such that

$$(x_B, y_B) = \arg\left[\max_{a(\vec{x}) \le a_o} p(\vec{x})\right] \tag{11}$$

Following from (3) and (4), the level set $L_a(p) = \{\vec{x} \in X : a(\vec{x}) = a_o\}$ has a corresponding $L_C(p) = \{\vec{x} \in X : p(\vec{x}) = p_o\}$ which is a Pareto solution at the boundary point (x_B, y_B). The expression in (10) can be extended to functions of two variables.

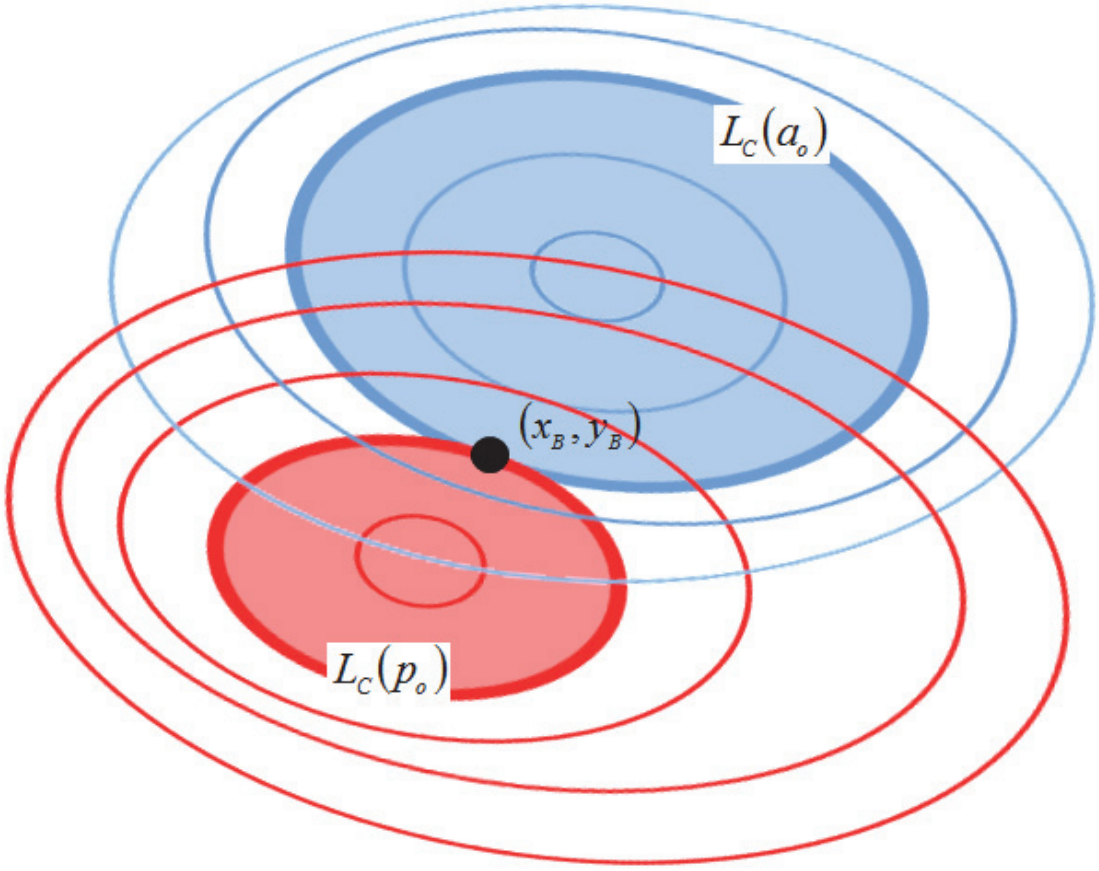

Figure 3.4: Level Sets $L_C(p_o)$ and $L_C(a_o)$ Form a Pareto Solution (x_B, y_B) For Objectives $p(\vec{x})$ (red) and $a(\vec{x})$ (blue)

Evaluating the location of (x_B, y_B) can be accomplished by weighting each function so that the peak of the cusp formed between $p(\vec{x})$ and $a(\vec{x})$ is at that location. Using the parameterized form in (10),

$$(x_B, y_B) = \arg\left(\max\left(\min\left(\alpha p(\vec{x}), (1-\alpha) a(\vec{x})\right)\right)\right). \tag{12}$$

A property of level sets is that for a function $f: X \to \mathbb{R}$, the gradient of f at the point $x \in X$ such that $\nabla f(x) \perp L_C(x)$. The gradients at (x_B, y_B) for the objective functions $p(\vec{x})$ and $a(\vec{x})$ are given by (13) and (14).

$$\nabla p(x_B, y_B) = \begin{bmatrix} \dfrac{\partial p(x_B, y_B)}{\partial x} \\ \dfrac{\partial p(x_B, y_B)}{\partial y} \end{bmatrix} \tag{13}$$

$$\nabla a(x_B, y_B) = \begin{bmatrix} \dfrac{\partial a(x_B, y_B)}{\partial x} \\ \dfrac{\partial a(x_B, y_B)}{\partial y} \end{bmatrix}. \tag{14}$$

Furthermore, the gradients are for the two level sets are oriented in the opposite direction at their [52] intersection and thus satisfy

$$\alpha \nabla p(x_B, y_B) + (1-\alpha) \nabla a(x_B, y_B) = 0. \tag{15}$$

Note that the α in expression (15) is different from the previous use, and instead represents an arbitrary constant. The expression in (15) is only valid for the intersection between the level curves of $L_c(p_o)$ and $L_c(a_o)$. The Pareto front is not a function of the measurement units as long as the transformation between one unit and another is strictly increasing. Measurements of power ratios, for example, will yield the same Pareto

contour as using the log of the ratios. The method for generating the Pareto front will now be applied to load-pull data extracted for both simulation and measurement.

3.2 Pareto Front for Simulated and Measured Load-Pull Contours

Identifying the Pareto front for amplifier design will allow for an optimal tradeoff to be made between two objectives. The approach taken is to apply Pareto analysis to previously measured load-pull data. The optimal tradeoff solutions mapped to the complex impedance plane can serve as a design guide for the linearity and efficiency tradeoff in nonlinear amplifier operation. Assuming that these contours are unimodal and fulfill the definition of convexity given by (1), the Pareto tradeoff curve will yield solutions which provide a unique optimum tradeoff between two objectives. Consider the simulation of an HBT amplifier model using ADS in Figure 3.5 under a CDMA2000 excitation. The bandwidth chosen for this simulation is 1.2288 MHz. This waveform demonstrates the applicability of Pareto analysis to a broad class of wideband signals.

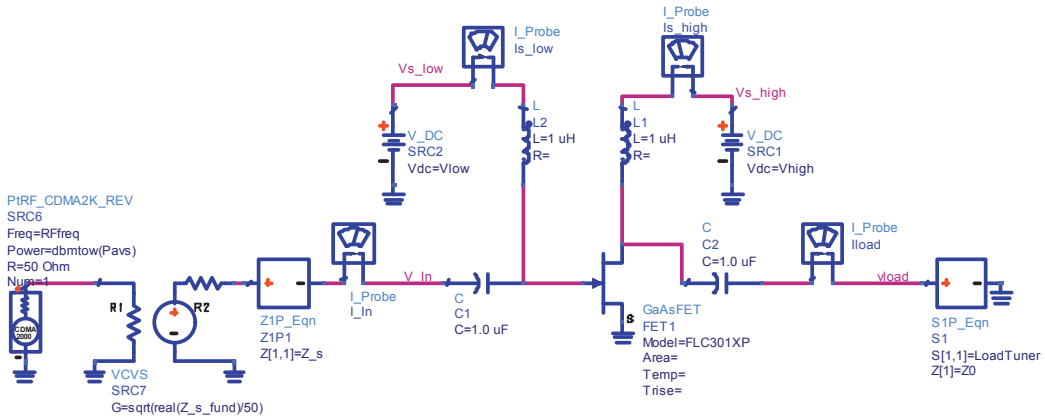

Figure 3.5: Circuit Schematic for HBT Circuit Envelope Simulation

A Circuit Envelope Simulation is used to evaluate the load-pull contours of the amplifier model, which is driven into the nonlinear operating region at an input power of

19 dBm. The characteristics measured for this test are PAE and ACPR, where the ACPR channels have a 30 kHz bandwidth and are offset 755 kHz from the 825 MHz carrier. Figure 3.6 shows the load-pull contours for PAE and ACPR with a 1% and 0.5 dB spacing respectively. The contours for PAE and ACPR are shown to have extrema at locations $\Gamma_L = 0.67\angle 169.42$ and $\Gamma_L = 0.83\angle -174.22$ respectively. A Pareto front generated between the two objectives reveals an optimal tradeoff path. This path allows a designer to choose a point along the Pareto line which optimizes between ACPR and PAE.

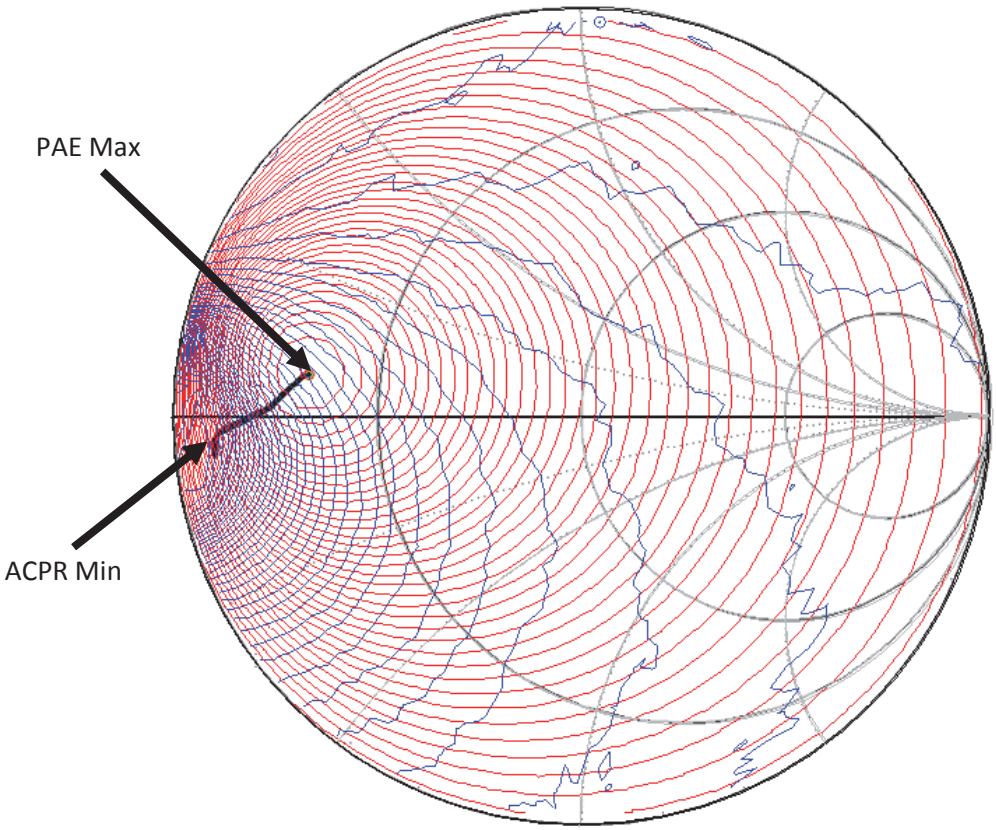

Figure 3.6: Simulated Load-Pull Contours for PAE (red) and ACPR (blue) with Pareto Path (black)

Although evaluating the Pareto front for measurement and simulation data is very similar, the effects of measurement noise and sampling of impedance points can affect

the results. A load-pull measurement is performed on an amplifier at 2 dB compression under a radar chirp excitation. Contours for the two objective functions, ACPR and PAE, were measured from a dense grid of impedances on the Smith chart, as shown in Figure 3.7.

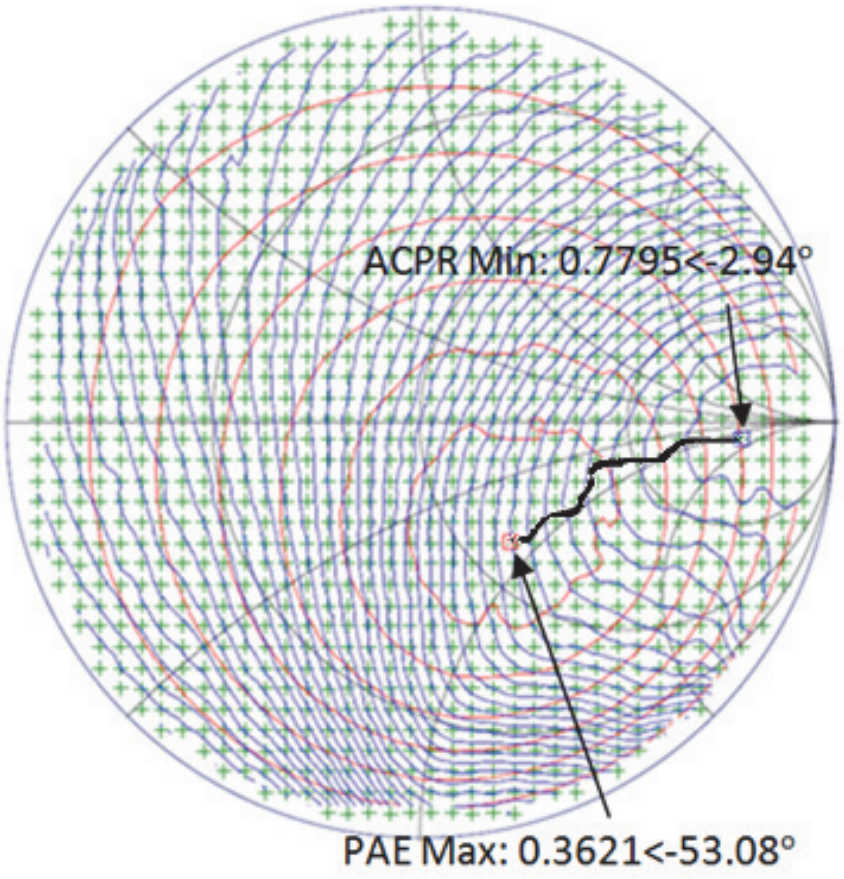

Figure 3.7: Amplifier Load Pull for PAE (red) at 1% Contour Spacing and ACPR (blue) at 0.5dBc Contour Spacing with Pareto Path (black)

The PAE and ACPR extrema are a significant distance apart, indicating that a design decision would need to be made for optimizing linearity and efficiency for this device. Applying the Pareto optimization for quasi-convex sets shows the tradeoff curve. The quantized data was interpolated and smoothed in order reduce the effects of system

noise. Smoothing the measurement data slightly changes the Pareto front due to changes in the original objective functions, but does not significantly affect the set topologies.

3.3 Conclusion

A method for mapping for mapping a Pareto tradeoff curve between linearity and efficiency has been shown. This technique utilizes load-pull measurements in order to map the tradeoff curve to the Smith chart. The solutions along this Pareto line are solutions for amplifier reflection coefficients which negotiate a weighted tradeoff between linearity and efficiency. The method shown for solving for a Pareto tradeoff for load-pull objectives depends upon their topology. These objectives often take the form of convexity defined in (1), where the set of Pareto solutions between them can be found using (12). These Pareto optimization routines provide an a priori design tradeoff between linearity and efficiency for amplifier load impedance design. Adaptive radar systems, however, require this tradeoff to be negotiated in real time depending on external constraints. The next section presents a method for approximating the Pareto front for linearity and efficiency using real-time intelligent search techniques.

CHAPTER FOUR

Sequential Peak Search Algorithm for Affine Pareto Tracing

The tradeoff between linearity and efficiency mentioned in Chapter 2 presents a problem for high power radar transmitters with a regulated spectrum for their emissions. Waveform distortions, which have been shown to result from nonlinear amplifier operation, can produce interference in adjacent frequency bands. As described in Chapter 2, reducing the input power to the amplifier can result in operation that is closer to linear and reduce the spectral spreading, but this also lowers the efficiency. One the other hand, driving the amplifier near saturation to meet high operating efficiency may result in violation of spectral mask requirements. Load-pull has been shown to be a useful tool for designing amplifier matching networks for the linearity and efficiency tradeoff.

Because of the changing nature of wireless spectrum allocation, radar systems may soon be forced to operate in a dynamic spectrum access environment, with changing spectrum requirements and perhaps being required to perform real-time shifts in operating frequency. Future radar systems must be able to adapt in real-time to meet changing spectrum requirements and switch between operating bands; this will require real time re-optimization of the amplifier load impedance and the waveform. Qiao *et al.* [53] have demonstrated on-chip impedance optimization for communication transmitters, and Baylis *et al.* [54], as well as de Hek [55] and Perlow [56] have demonstrated peak-search load-pull algorithms for output power optimization. As such, real-time matching techniques and intelligent algorithms show excellent promise for the optimization radar amplifier circuitry using real-time load-pull measurements. This chapter presents a

method for approximating the Pareto optimal solutions for linearity and efficiency using a combined peak search method. The concept of adaptive load tuning for radar systems will be discussed, followed by a comparison of the steepest descent search path to the Pareto curve generated between two objectives.

4.1 Augmenting Adaptive Radar Transmitters

Modern radar transmitters are required to fulfill multiple conflicting constraints while maintaining optimal detection capabilities. As bandwidth for radar systems decreases due to economically driven wireless applications, the allowable interference produced by the radar transmitters will also decrease. As discussed in Chapter 2, radar systems are often driven into saturation where nonlinear amplifier effects are dominant. Using a static output matching impedance for the design of a power amplifier can be chosen to maximize the efficiency of the device. An adaptive radar transmitter, however, must be able to adjust its waveform and circuitry according to external influences such as spectral mask. Additionally, multiple waveforms may need to be implemented on the same radar system for increased target detection [57], and cause the amplifier output matching network to be suboptimal for desired performance.

The method proposed is to augment the concept of adaptive radar transmitters by introducing a tunable load impedance network at the output of the radar system. The ability to digitally define modulated signals is combined with the functionality of impedance tuning through load-pull techniques. Figure 4.1 shows a concept diagram of an adaptive radar transmitter.

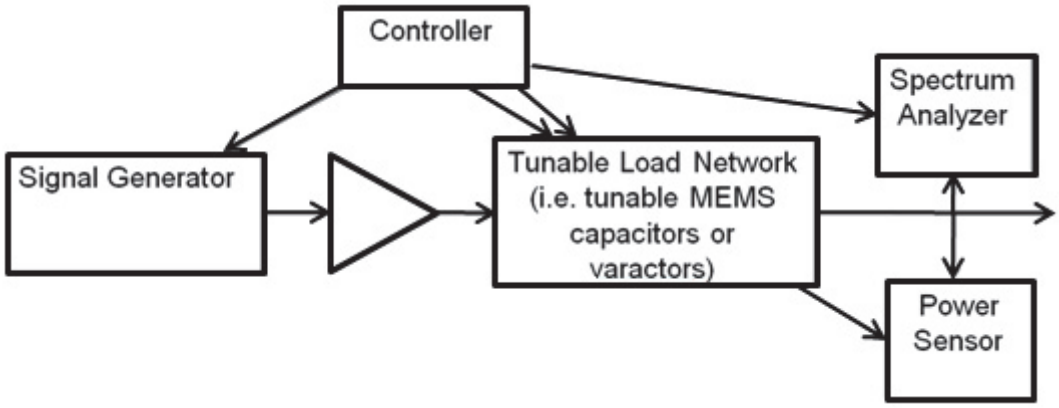

Figure 4.1: Adaptive Radar Transmitter with Tunable Load Impedance

The main components of this setup consist of a signal generator for producing modulated signals, a tunable impedance network, a central controller, and feedback using a spectrum analyzer and power sensor. Unlike a traditional load-pull measurement, the system is directed by a central controller which receives feedback data acquired for PAE and ACPR. The central controller is responsible for waveform generation, impedance tuning, data collection, and making design decisions which impact system performance. These decisions are based on the current system requirements for linearity and efficiency, and implemented as changes in the waveform and/or load reflection coefficient at the amplifier output. The robustness of this concept overcomes limitations of a priori design by allowing the amplifier load impedance to be adjusted for multiple operating points and spectral mask constraints. However, another constraint for adaptive systems is the speed at which the controller converges on the optimal performance setting. Assuming a fixed waveform, identifying the optimal load impedance for a tradeoff between PAE and ACPR with a small number of measurements is critical. Designing intelligent search techniques for the load pull provides a way to drastically reduce the number of measurement queries required, and is discussed in the next section.

4.2 Sequential Peak Search Algorithm

The study of typical load-pull contours in Chapters 2 and 3 indicate that the objectives are often realized as unimodal, convex or quasi-convex sets. The peaks of these sets correspond to locations which best optimize either set. Using the scheme shown in Figure 4.1, the central controller is responsible for locating the optimal reflection coefficient for a tradeoff between PAE and ACPR. An unbiased search algorithm is implemented using the steepest ascent method to locate these reflection coefficients on the complex impedance plane. The gradient search method has been suggested in [47, 58] for finding the peak of unimodal functions. This method has been explored in [54, 59] for optimizing a single amplifier objective through load impedance tuning. Since the reflection coefficient Γ is a complex number, it can be analyzed as a two dimensional vector such that $\vec{\Gamma} = \begin{bmatrix} x \\ y \end{bmatrix}$ where $x, y \in \mathbb{R}$. The search begins at an arbitrary point Γ_o on the complex impedance plane and calculates the gradient at that point. This calculation is made by taking two additional measurements at points Γ_r and Γ_i neighboring the initial location at a predetermined distance D_n such that

$$\vec{\Gamma}_r = \begin{bmatrix} x_r + D_n \\ 0 \end{bmatrix} \tag{1}$$

$$\vec{\Gamma}_i = \begin{bmatrix} 0 \\ x_i + D_n \end{bmatrix}. \tag{2}$$

The measured magnitudes at the measurement locations, which are $p(\Gamma_o)$, $p(\Gamma_r)$ and $p(\Gamma_i)$, will be used to approximate the gradient in a neighborhood around Γ_o shown in Figure 4.2.

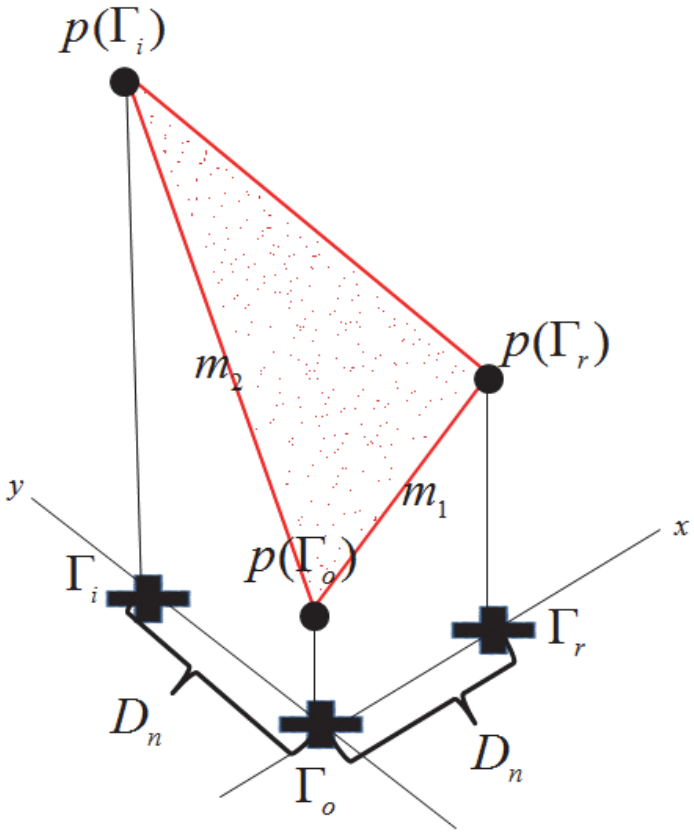

Figure 4.2: Topology of Neighboring Points for Gradient Calculation

The additional neighboring points are equidistant from the initial point, and lines drawn the initial power value and neighboring values form slopes m_1 and m_2. These slopes represent the rate of linear increase between the initial magnitude of p and the neighboring points. A plane shown in (1) is fit to the three measured points to solve for the direction of steepest ascent.

$$\Delta p\left(\Delta\vec{\Gamma}_r, \Delta\vec{\Gamma}_i\right) = m_1\Delta\vec{\Gamma}_r + m_2\Delta\vec{\Gamma}_i \tag{3}$$

where Δp, $\Delta\Gamma_r$, and $\Delta\Gamma_i$ refer to the change from their starting values at Γ_o. The direction of greatest increase is calculated in [54] along a line following the gradient. The algorithms then moves a certain step distance D_S from the initial point as shown in Figure 4.3.

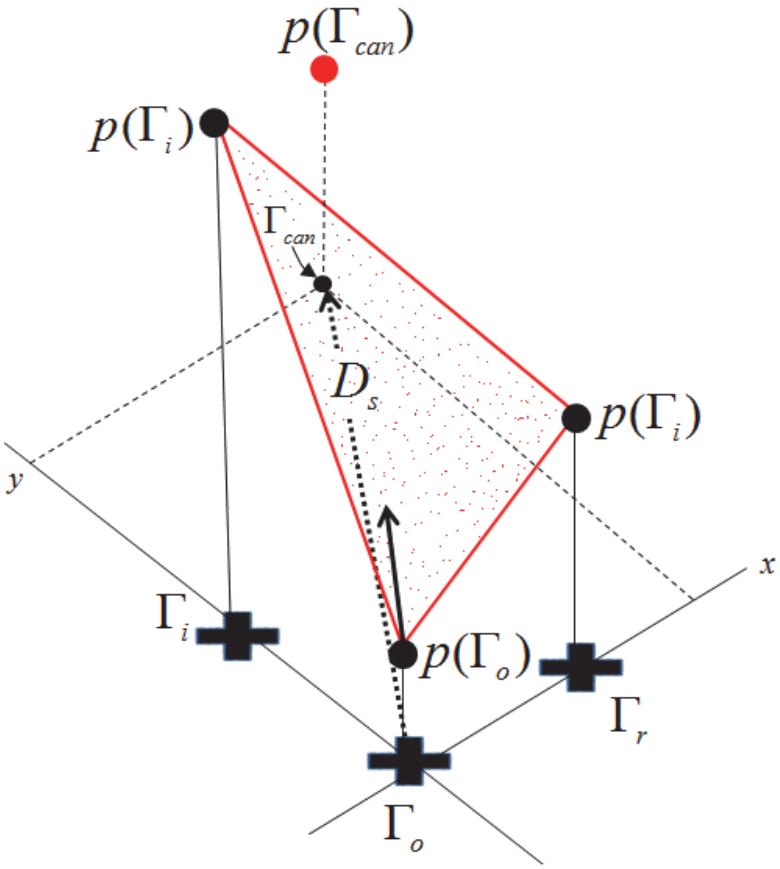

Figure 4.3: Step in the Direction of Steepest Ascent

The new location is measured for the current objective and the process repeats if the new magnitude is higher than that of the initial point. The step size decreases to one-third of its original value if the new location's magnitude is lower than that of the initial point. The reduction in step size indicates that the objective peak has been overshot and provides a way to converge on the peak with precision. This process continues until the step size becomes less than the neighboring point distance, in which case the steepest ascent algorithm halts. The point Γ_f at which the steepest ascent iterations cease and associated neighboring points map a region of uncertainty as to the true location of the objective peak. The extent of this region depends on the neighboring point distance, which sets the resolution of the search. Approximating this peak is accomplished by

taking three additional measurements and performing a least squares fit to all six points [55]. The fit ideally results in a paraboloid that has a peak at the approximate location of the true objective peak, and is shown in Figure 4.4. Evaluating the gradient of the paraboloid and solving for the point at which the gradient equals zero yields the maximum at location Γ_{opt}.

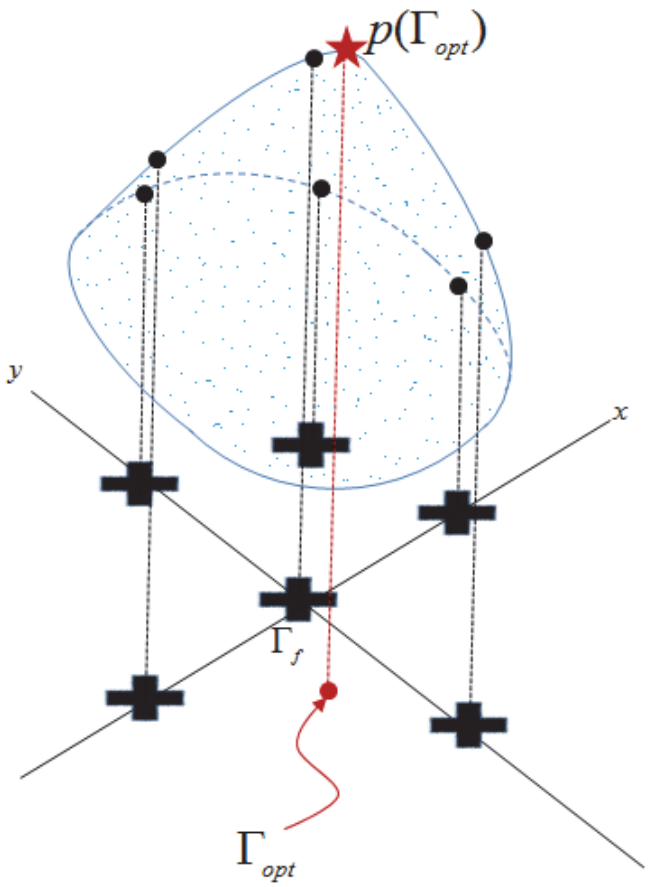

Figure 4.4: Paraboloid Fit (blue) to Six Points Using Least Squares and Peak Location (red)

The combined peak search algorithm for finding PAE and ACPR modifies this steepest ascent search by performing two searches consecutively. The algorithm executes a steepest ascent for PAE as explained previously, finding the location of maximum PAE, $\Gamma_{opt,P}$, and the magnitude at that point $p(\Gamma_{opt,P})$. Starting from $\Gamma_{opt,P}$, an additional

steepest descent search begins for the ACPR optimum $\Gamma_{opt,a}$. This concept is illustrated in Figure 4.5 for arbitrary unimodal PAE and ACPR sets.

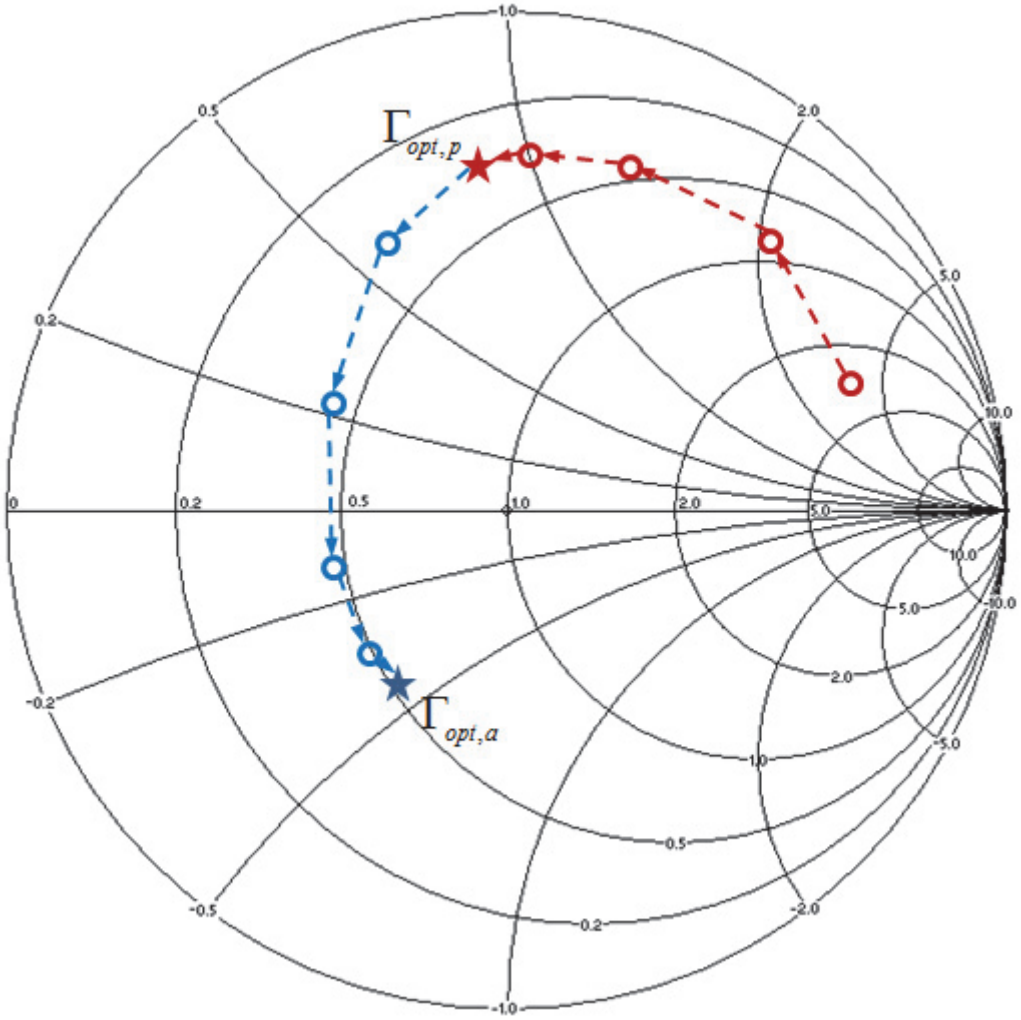

Figure 4.5: Combined Peak Search for PAE (red) and ACPR (PAE)

Performing the second steepest descent algorithm for ACPR has two important ramifications for adaptive radar. One benefit of this algorithm is the ability to design between two conflicting objectives in real time. An example of this would be to set an ACPR constraint, and perform a steepest descent algorithm going toward the ACPR optimum until the limit is reached. Truncating the steepest descent before the ACPR optimum is reached prevents needless reduction in PAE incurred when improving ACPR

beyond the requirements. The second development concerns the path the steepest descent algorithm follows. Chapter 3 discussed a Pareto path between PAE and ACPR which provides an optimal tradeoff between the two objectives. The questions of whether the steepest descent path for ACPR from the PAE optimum location approximates the Pareto path will be discussed in the next section.

4.3 Using Steepest Descent as Affine Approximation to Pareto Tradeoff Curve

When executing the steepest descent search of the routine (from the PAE optimum toward the ACPR optimum), the search traces a path between the optimum location of the two objectives. How closely this path approximates the Pareto curve is based upon the nonlinearity of the device characteristics and the search parameters. The steepest descent search is based on a calculation of the gradient at an initial search point similar to the steepest ascent algorithm described in the previous section, so it is desired to demonstrate under what conditions the Pareto curve proceeds in the direction of the gradients. Consider the Pareto curve between two characteristics for PAE, $p(\vec{\Gamma}_B)$, and ACPR, $a(\vec{\Gamma}_B)$, both functions of the two-dimensional position vector $\vec{\Gamma}_B = \begin{bmatrix} x_B \\ y_B \end{bmatrix}$. From Chapter 3, it was shown for load-pull contours that at the intersection point x_B between two level sets for PAE and ACPR that

$$\alpha \nabla p(x_B, y_B) + (1-\alpha)\nabla a(x_B, y_B) = 0. \tag{4}$$

As previously discussed, (4) demonstrates that, at a point on the Pareto curve, the gradients are collinear and pointing in opposite directions. This characteristic occurs because limitations on the value of α to be between 0 and 1 show

$$\nabla p(\vec{\Gamma}_B) = -\frac{(1-\alpha)}{\alpha}\nabla a(\vec{\Gamma}_B) \tag{5}$$

Assume that the characteristics p and a are both affine, at least in a region surrounding Γ_B, a point on the Pareto curve. An affine approximation for both functions can be defined as

$$a\left(\vec{\Gamma}_B + \Delta\vec{\Gamma}\right) \approx a\left(\vec{\Gamma}_B\right) + \nabla a\left(\vec{\Gamma}_B\right) \cdot \Delta\vec{\Gamma} \tag{6}$$

and

$$p\left(\vec{\Gamma}_B + \Delta\vec{\Gamma}\right) \approx p\left(\vec{\Gamma}_B\right) + \nabla p\left(\vec{\Gamma}_B\right) \cdot \Delta\vec{\Gamma} \tag{7}$$

where $\Delta\vec{\Gamma} = \begin{bmatrix}\Delta x \\ \Delta y\end{bmatrix}$ is a small two dimensional step in the direction of the gradient for either objective. Equations (6) and (7) show that $a\left(\vec{\Gamma}_B + \Delta\vec{\Gamma}\right)$ and $p\left(\vec{\Gamma}_B + \Delta\vec{\Gamma}\right)$ are related for cases where the affine approximation holds true. This consideration leads to the questions of whether some α' exists such that

$$\nabla p(\vec{\Gamma}_B + \Delta\vec{\Gamma}) = -\frac{(1-\alpha')}{\alpha'} \nabla a\left(\vec{\Gamma}_B + \Delta\vec{\Gamma}\right). \tag{8}$$

If (8) is true, then the point $\vec{\Gamma}_B + \Delta\vec{\Gamma}$ is also on the Pareto curve. The values of the two functions and their gradients must first be evaluated at the specific coordinate vector $\vec{\Gamma}_B$. This procedure allows the right sides of (6) and (7) to be numerically calculated. Taking the gradient of (7) yields

$$\nabla p\left(\vec{\Gamma}_B + \Delta\vec{\Gamma}\right) = \nabla[p\left(\vec{\Gamma}_B\right)] + \nabla\left(\nabla p\left(\vec{\Gamma}_B\right) \cdot \Delta\vec{\Gamma}\right). \tag{9}$$

Note that $\nabla[p\left(\vec{\Gamma}_B\right)]$ in the first term on the right of the equals sign occurs at point, and thus is the gradient of a constant with numerical components and therefore is zero. An assumption is made that the affine approximation is sufficiently accurate so that the second gradient is approximately zero. Inside the parentheses of the second term, however, is the gradient of p evaluated at the point Γ_B. This operation results in a vector

with components that are the partial derivatives of p with respect to x and y at the point Γ_B in (10).

$$\nabla p\left(\vec{\Gamma}_B\right) = \hat{x}\frac{\delta p}{\delta x}\left(x_B, y_B\right) + \hat{y}\frac{\delta p}{\delta y}\left(x_B, y_B\right) \tag{10}$$

Inserting the results from (10) into (9) gives

$$\nabla p\left(\vec{\Gamma}_B + \Delta\vec{\Gamma}\right) = \nabla\left(\frac{\delta p}{\delta x}\left(x_B, y_B\right)\Delta x + \frac{\delta p}{\delta y}\left(x_B, y_B\right)\Delta y\right). \tag{11}$$

The gradient requires derivatives to be taken of a scalar expression containing Δx and Δy. These variables can be rewritten in terms of x and y as follows:

$$x = x_B + \Delta x \tag{12}$$

$$y = y_B + \Delta y\,. \tag{13}$$

Because x_B and y_B are specific values of x and y, they are constants for purposes of differentiation. This means that

$$dx = d\Delta x \tag{14}$$

$$dy = d\Delta y. \tag{15}$$

This means that a derivative with respect to x is the same as the derivative with respect to Δx, and a derivative with respect to y is the same as a derivative with respect to Δy. Using this in (11) gives the following for the gradient of p at the new point:

$$\nabla p\left(\vec{\Gamma}_B + \Delta\vec{\Gamma}\right) = \hat{x}\frac{\delta p}{\delta x}\left(x_B, y_B\right) + \hat{y}\frac{\delta p}{\delta y}\left(x_B, y_B\right) = \nabla p\left(\vec{\Gamma}_B\right). \tag{16}$$

The expression in (16) shows that, when the surface p is affine, that the gradient at another point along the line established by the gradient taken at an original point is the

same as the gradient at the original point. The same is also true for the surface a such that

$$\nabla a\left(\vec{\Gamma}_B + \Delta\vec{\Gamma}\right) = \nabla a\left(\vec{\Gamma}_B\right). \tag{17}$$

This comparison shows that the relationship between the gradients at the new point is exactly the same as at the original point if both surfaces are affine:

$$\nabla a(\vec{\Gamma}_B + \Delta\vec{\Gamma}) = -\frac{(1-\alpha')}{\alpha'}\nabla p\left(\vec{\Gamma}_B + \Delta\vec{\Gamma}\right). \tag{18}$$

We have confirmed that (8) is true in this case with $a = a'$. Assuming cases where the affine approximation holds, the next step in a steepest descent walk from a point on the Pareto surface results in a point which is also on the Pareto surface since the gradients are perpendicular for both criterion surfaces. The case where Γ_B happens to be the optimum of criterion p indicates $\alpha = 1$ in (4) and the gradient $\nabla p(\Gamma_B) = \bar{0}$, the zero vector. Regardless of the value of $\nabla a(\Gamma_B)$, (5) is satisfied and this point is on the Pareto line. Additionally, the case where two characteristics p and a are on the Pareto path and a nearby point is chosen in the direction of one of the gradients (direction of steepest descent), the next point is also on the Pareto path if both of the characteristics are linear.

A closer look at the derivation reveals that the gradients never change direction as the steepest descent walk is carried forward from one point to the next. The progression would continue from one maximum to the other along the Pareto line. This case is a unique contour type that would only be likely to occur only in linear devices. However, if both p and a are re-measured at each point, then the approximation becomes *piecewise* affine rather than strictly affine, and the results will better approximate the actual characteristics in nonlinear situations. The Pareto load-pull search is an attempt to map the Pareto line based on a piecewise affine approximation. The search begins at the

optimum impedance for power-added efficiency (PAE) and proceeds toward the optimum impedance for adjacent-channel power ratio (ACPR). This steepest descent-walk will follow the Pareto path only if both criterion characteristics can be reasonably approximated as linear over the step size.

A problem with the piecewise affine approximation is that the error in the approximation causes the search to leave the Pareto path, with no way to regain position on the path. A nudge factor is suggested for future work, based on the difference of the two characteristics' gradients at each approximation point of the search, to keep the search near the Pareto path, ensuring optimum PAE is achieved in meeting ACPR requirements.

4.4 Conclusion

A Pareto-search algorithm for PAE and ACPR has the promise to greatly extend adaptive radar capabilities by allowing the circuitry to adapt for different amplifier spectrum requirements and frequency bands. This real-time reflection-coefficient optimization is broadly applicable to many devices and provides a flexible approach that can be adopted in a wide range of conditions. The key to achieving robust applicability is the use of a controller to direct the waveform creation, impedance tuning, and measurements to make intelligent design decisions. The combined peak search algorithm, under the assumption of objective unimodality, is an unbiased empirical search that proceeds without using knowledge of device linear or nonlinear network parameters. If such knowledge is available, the search can likely be performed with even fewer queries by intelligently selecting the starting point and the search-distance and neighboring-point-distance parameters.

The affine approximation to the Pareto curve using steepest descent provides a method for finding an optimal tradeoff between PAE and ACPR in a real time impedance matching network. Under an affine approximation for both surfaces, the gradients will be collinear at a nearby point in the direction of the gradient at the first point. This means that if one point lies on the Pareto curve, the next point in a steepest descent search from one optimum to the other, to a first-order approximation, will also lie on the Pareto curve. A piecewise affine approximation will proceed from one optimum to the other only if a piecewise affine approximation to the surface is accurate. Such consideration usually dictates that the step size for the search between the PAE and ACPR optimum points be small enough that the piecewise linear approximation will be reasonable, while keeping it large enough so that the total number of experimental queries is relatively small. The next chapter discusses the implementation of this algorithm in simulations and measurements.

CHAPTER FIVE

Reconfigurable Radar Test Bench

The implementation of the adaptive radar transmitter in Chapter 4 incorporates several common operations to load-pull measurements. These procedures include waveform generation, impedance tuning, and measurements for spectrum and output power. An adaptive approach, however, contains an additional decision making element that expands the use of load-pull beyond device characterization. The load-pull for measurement becomes a load-pull for design or real-time optimization by the incorporation of an intelligent controller. This controller implements optimization methods such as steepest ascent to impedance tuning in order to obtain solutions to multi-objective amplifier design. Additionally, the combined peak search algorithm enables the steepest ascent algorithm between two objectives to approximate their Pareto front. This chapter discusses an implementation of the combined peak search algorithm in software and with a load-pull test bench.

5.1 Sequential Peak Search Algorithm Implementation

The objective of the combined peak search algorithm is to find the amplifier load reflection coefficient providing the PAE and ACPR necessary based on constraints in order to optimize for linearity and efficiency. The algorithm presented in this thesis searches for maximum PAE, then proceeds toward the ACPR optimum until the spectral constraints are met. The central controller for the adaptive radar system in Figure 4.1 of Chapter 4 plays a key role in implementing this algorithm. An unconstrained search such

as steepest ascent must be able to converge on the optimal impedances for PAE and ACPR without a priori knowledge of the device fitness landscape. The central controller generally applies the same algorithm depending on whether it is implemented through software or on a test bench. This decision making unit is responsible for executing software which realizes the intelligent algorithm being implemented. The upper level block diagram for the implementation in this chapter is shown in Figure 5.1.

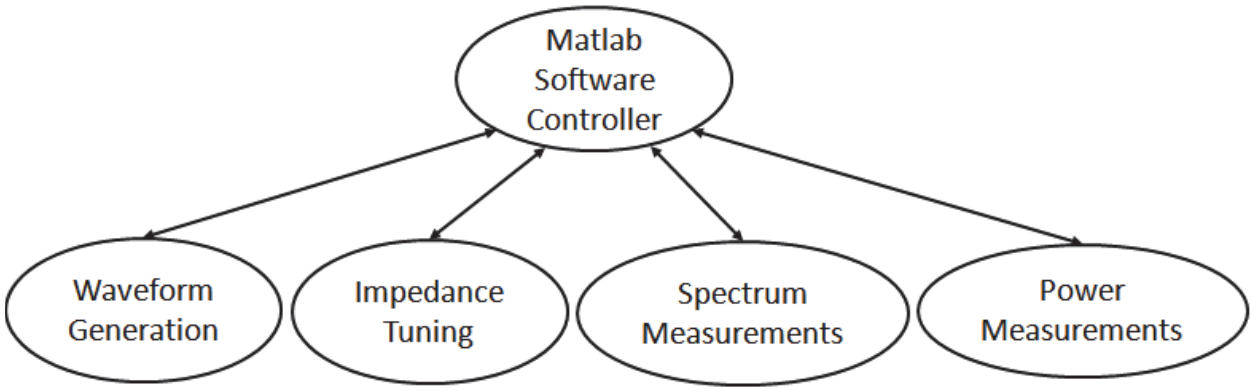

Figure 5.1: Control Diagram for PAE and ACPR Search Reprinted from [60]

The primary software used for both the software and test bench implementations of the combined peak search is the MATLAB computing environment. One of the primary reasons for choosing this programming language is the ease with which communication is achieved with external devices. The software which directs the combined peak search algorithm must be able to execute all stages of the algorithm, including waveform generation, impedance tuning, spectrum analysis, and power sensing. Additionally, MATLAB possesses the ability to interface with software such as Advanced Design System (ADS) and Maury Automated Tuner Software (ATS) in order to direct the measurement. Communication by MATLAB with third-party software is handled through external libraries, which MATLAB is able to invoke and execute. One

level below the MATLAB controller block in Figure 5.1 are the devices through which the algorithm is implemented. The first block consists of an arbitrary waveform generator, which is a digital transmitter used to create various modulated signals. The impedance tuning block sets the output impedance of an amplifier for the duration of the algorithm, and is used as the primary knob for adjusting linearity and efficiency. Data feedback is essential to automating the algorithm using this setup, and is implemented through the use of spectrum and power measurements. Once communication is achieved between the blocks in Figure 5.1, the combined peak search algorithm is implemented in MATLAB. Figure 5.2 shows the flow diagram of this algorithm as written in the script.

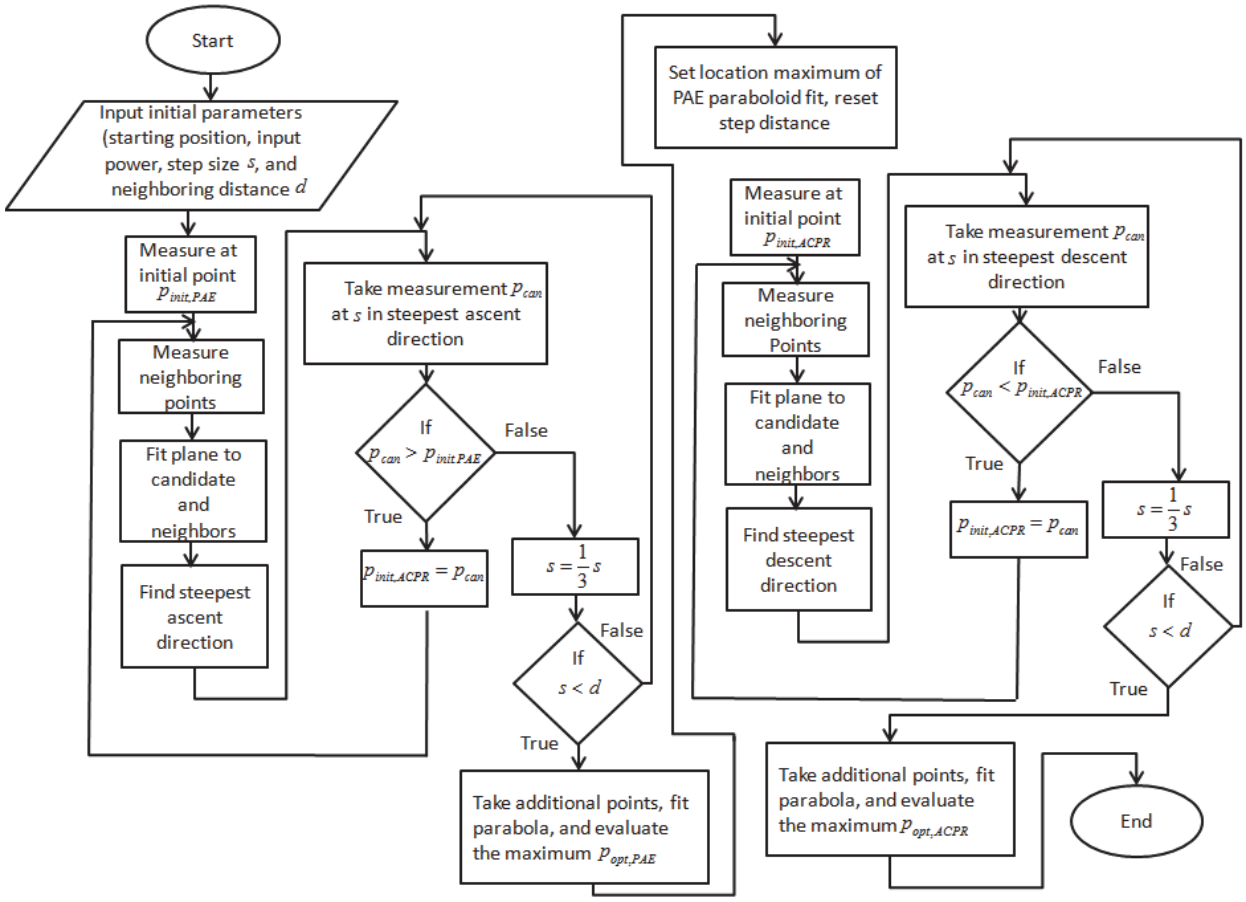

Figure 5.2: Flow Diagram for Combined Peak Search Algorithm

The algorithm begins by asking the user for a starting reflection coefficient, step size, and neighboring point distance for gradient calculation. Any arbitrary starting point can be selected given the condition that the search objective is unimodal. This initial point $p_{init,PAE}$ is the starting point for the PAE steepest ascent search, and is measured for its respective magnitude. A plane needs to be fit to this initial point and two neighboring points in order to find the gradient, so two additional points are measured at the neighboring point distance D_n. This distance directly influences the resolution of the search. Points which lie between $p_{init,PAE}$ and D_n on the Smith Chart will be neglected in the gradient calculation. Figure 5.3 shows the measurement point topology for neighboring point distance D_n and the step distanceD_s.

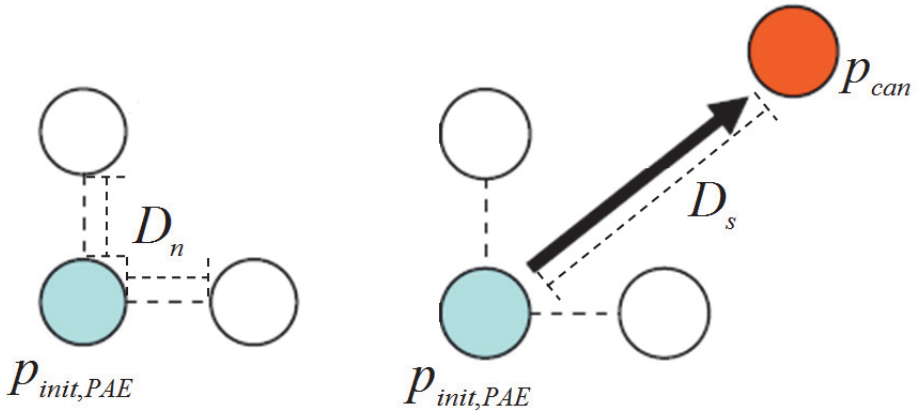

Figure 5.3: Influence of Neighboring Point Distance and Step Distance on Measurement Topology Reprinted from [61]

Once a plane is fit to the three measured locations, the gradient is calculated and the algorithm measures a point for PAE in the direction of steepest ascent with a step size of D_s. The step size directly influences the speed of the search, and will be an important resolution factor in the steepest descent for ACPR and Pareto front approximation. The measured point p_{can} at a distance D_s is compared with $p_{init,PAE}$ for determining when to

decrement the step size, which is used to increase measurement accuracy. A candidate value higher than the initial value indicates that the PAE peak has not been reached, and the algorithm continues until this condition is not met. Measuring the candidate value to be lower than the initial value implies that the PAE peak has been overshot, and the step size is reduced to one-third of its original value. Once the step size is reduced to less than the neighboring point distance, the steepest ascent algorithm comes to a halt. This is due to the assumption that the PAE maximum now lies within the region spanned by the neighboring point distance. Approximating the peak over this region requires a least squares fit to a total of six points including the final measured point and respective neighboring points. Measuring three additional points for PAE at the neighboring distance allows a paraboloid to be fit to the data. This function is desired since it provides a single global maximum. Taking the gradient of this paraboloid yields the approximate location of the PAE maximum. A second steepest descent algorithm is carried out for the ACPR optimum reflection coefficient beginning at the optimum reflection coefficient for PAE. The algorithm generally follows same procedure for the PAE search with a couple key exceptions. The purpose of the steepest descent algorithm for ACPR, as stated in Chapter 4, is to provide a piecewise affine approximation of the Pareto front between the PAE and ACPR objectives. This necessitates that the step size be relatively small for the steepest descent in order for the algorithm to best approximate the tradeoff curve. The ACPR minimum is sought, so the ACPR search algorithm is a steepest descent algorithm. The minimum point for ACPR is evaluated in a similar fashion to that of PAE, except with aim of achieving a global minimum. The algorithm terminates once the locations for optimum PAE and ACPR have been identified. The algorithm in Figure 5.2 can be easily modified to end at the desired ACPR constraint

instead of tracing the Pareto curve, which is practical in terms of maximizing PAE for an ACPR constraint in a radar system. Implementing this limit reduces the number of measurement queries required to trace the entire Pareto curve. This system can be applied to both software simulations for load-pull and a physical load-pull test bench, instantiations of which are explained in the following sections.

5.2 Reconfigurable Software Test Bench

The algorithm for combined peak search can be demonstrated fully in software using the RF design software ADS and the MATLAB computing environment. This method relies on ADS to perform simulated load-pull measurements for modulated signals while MATLAB performs the intelligent search. The simulated load-pull measurement consists of a circuit envelope simulation for impedances of interest. Proper setup of the circuit envelope simulation is essential to producing accurate load-pull contours for modulated signals. The technique used combines both time and frequency domain analysis of the waveform [62]. Harmonic balance is another technique for evaluating amplifier characteristics, but becomes computationally intensive as signal complexity increases. The circuit envelope simulation overcomes this limit by performing successive harmonic balance over specified time steps for the total defined time of the waveform. The harmonic balance generates Fourier series coefficients for time segments spaced Δt, over the total time duration of the waveform T. This process is shown in Figure 5.4 for an arbitrary modulated signal. The Fourier series coefficients for each of the time segments are used to solve for a time domain solution to the amplifier output waveform. Obtaining spectral information about the output signal is accomplished by performing a fast Fourier Transform of the data. This operation is particularly

important for simulating ACPR for load-pull. An important consideration in ensuring the spectrum is reported accurately is to design the time characteristics of the circuit

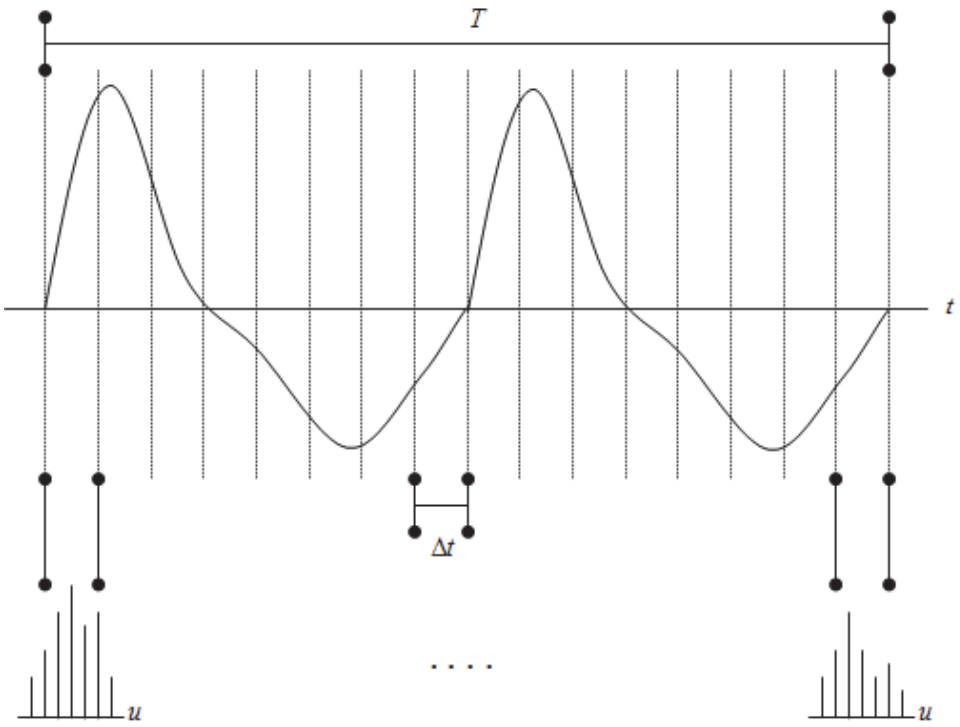

Figure 5.4: Performing Circuit Envelope Simulation for an Arbitrary Modulated Signal

envelope simulation according to the waveform being measured. The step time is inversely proportional to the bandwidth of the circuit envelope simulation. This requires that the signal be "sampled" fast enough such that the signal can be accurately approximated. The total time duration of the circuit envelope simulation is likewise inversely proportional to the frequency resolution of the signal. The circuit envelope simulation during a load-pull measurement is performed over load reflection coefficients of interest. This data is used to plot contours over the Smith Chart and provide an approximation of an amplifier model with a modulated signal excitation. Performing the combined peak search algorithm with ADS requires MATLAB to request input from the

user. The information gathered using ADS is relayed to MATLAB and results in further prompting by the algorithm script. This process is carried out until the condition is met in Figure 5.1. The use of software to implement the steepest ascent algorithm serves as a low cost evaluation of the algorithm effectiveness. Producing the algorithm on a test bench, however, is more complicated and is explained in the next section.

5.3 Adaptive Radar Test Bench

The combined peak search algorithm for linearity and efficiency optimization can be realized as an adaptive load-pull test bench. A basic load-pull setup contains many of the primary functions required for the algorithm, including measurements of output power and ACPR at various load impedances. Controlling the load impedance seen by a DUT is accomplished through the use of mechanical impedance tuners. The design is based on a "slide screw" concept, which adjusts the impedance by using a metal plunger and a 50 ohm air line [14]. These tuners are characterized to cover impedances which span the Smith Chart at certain frequencies of interest. The main software controller for this measurement is Maury ATS, which primarily drives the load impedance tuners and interfaces with the equipment in Figure 5.5. The functionality provided by MATLAB allows a direct interface to the external libraries of Maury ATS. These libraries allowed indirect control of equipment drivers such as the impedance tuners while retaining the functionality of the Maury ATS graphical user interface. The main functions provided by Maury ATS are adjusting the impedance for a particular measurement and controlling the settings of external hardware.

An arbitrary waveform generator, the Agilent 5182A, emits pre-programmed waveforms from MATLAB. This functionality allows for unique modulations to be generated using software, and further expands the adaptability of the platform. This

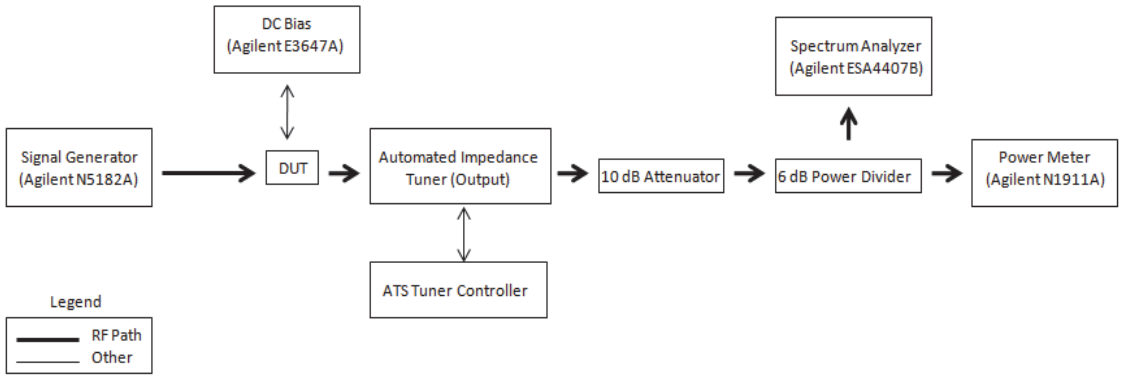

Figure 5.5: Reconfigurable Load Pull Measurement Setup Block Diagram Reprinted from [28]

waveform segment is unconverted to the desired carrier frequency and repeated continuously while the measurement is taking place. The RF emission passes through the device under test (DUT), impedance tuner, splitter, and ends at two distinct sensors. The splitter allows the simultaneous measurement of the spectrum and broadband output power simultaneously. The Agilent N1911A power meter measures the broadband output power of the DUT for calculating the PAE, whereas the Agilent E4407B spectrum analyzer detects the frequency spectrum for calculating ACPR. Once these values are measured for particular load impedances, the results are reported through Maury ATS to the MATLAB software.

One of the most important aspects of the measurement setup is determining the frequencies to be used to define the ACPR adjacent-channel boundaries. The ACPR measured depends on the bandwidth and center frequency of the channel on the modulated signal spectrum. The in-band and adjacent channel power values are measured by adding the measured power values within the specified channel over bandwidth. These values, which are used to form contours over the Smith chart during load-pull, may cause the combined peak search algorithm to take different paths for

identifying the tradeoff between PAE and ACPR. Correctly identifying the ACPR channels and bandwidth of interest is essential for achieving the desired unique solution using the combined peak search algorithm.

5.4 Conclusion

The combined peak search algorithm can be implemented in both software and as an adaptive radar test bench. The ability to interface to both platforms is afforded by the MATLAB computing environment. The software method utilizes ADS to produce simulated ACPR load-pull data using circuit envelope simulation. This provides a convenient way to evaluate the software algorithm for different devices, modulations, and circuit topologies. The adaptive test bench integrates the measurement capabilities of ACPR load-pull with control and automation of the algorithm through MATLAB. Control is accomplished by interfacing with the Maury ATS software through external libraries. The communication between these programs allows the built in Maury ATS functions to be directed by the algorithm script. The next chapter will discuss the results of tests performed for both software and test bench instantiations. These examples will demonstrate the ability of the algorithm to approximate the Pareto front between PAE and ACPR using a finite number of measurements.

CHAPTER SIX

Analysis of Sequential Peak Search Results

The results of the sequential peak search algorithm are validated by showing that several instantiations of the search converge to the PAE and ACPR impedances that are determined to be optimal by traditional load-pull measurements. Following the conceptual description in Chapter 4, the sequential peak search algorithm should first locate the optimum point for PAE. A steepest descent search will then proceed from the PAE optimum load reflection coefficient and iterate towards the ACPR optimum point. Additionally, the steepest-descent walk between the optima uses a small D_s in an effort to roughly approximate the same trajectory as the Pareto optimal path. The test bench in Chapter 5 enables the load impedance of a DUT to be maneuvered according to inputs received from a spectrum analyzer and wideband power sensor. A MATLAB programmed script realizes the sequential peak search algorithm by receiving feedback from the measurement equipment and decides the reflection coefficient of an impedance tuner at the DUT output. This chapter will show the results of the sequential peak search algorithm for a series of tuner impedance instantiations which are spread out along the Smith chart. Key factors such as number of measurements, standard deviation of final magnitudes, and the mean magnitude at these points are used to demonstrate the algorithm's effectiveness. A modification of the algorithm will also be shown which imposes a maximum limit on ACPR.

6.1 ADS Simulation of Sequential Peak Search Algorithm

A simulated sequential peak search algorithm is demonstrated for the ADS simulation in Figure 6.1. The simulation is for a GaAs FET device driven to its nonlinear operating point at an input power of 19 dBm under a CDMA2000 excitation. This source was chosen in order to demonstrate the applicability of the sequential peak search algorithm to a variety of wideband modulation schemes. An exhaustive simulated load-pull with 1127 simulated reflection-coefficient states was performed to obtain sufficient resolution and coverage of the amplifier behavior over the Smith Chart, where the optimum values and locations for PAE and ACPR are shown in Table 6.1.

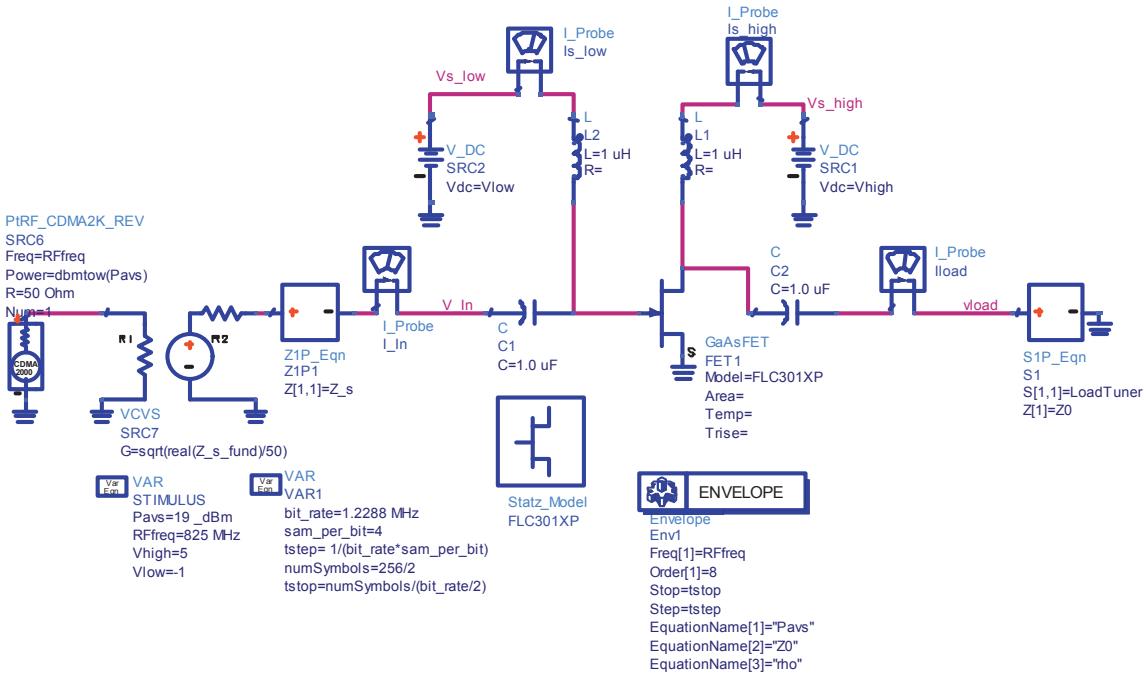

Figure 6.1: Circuit Diagram for ADS Load-Pull Simulation

Table 6.1: Simulated Load-Pull Data Standard

Data	Magnitude	Angle	Resistance (Ω)	Reactance (Ω)	Value
PAE	0.6703	169.4176	0.1990162	0.088974129	33.727071
ACPR	0.9403	-176.952	0.0307902	-0.026579888	-52.013813

Figure 6.2a demonstrates the steepest ascent algorithm for PAE starting at the reflection coefficient $0.9\angle 90^{o}$, and Figure 6.2b shows the location of the PAE maximum and contours. The contours are spaced 1% for PAE and 0.5 dBc for ACPR. The peak search algorithm for both PAE and ACPR requires certain considerations such as algorithm step size D_s and neighboring point distance D_n.

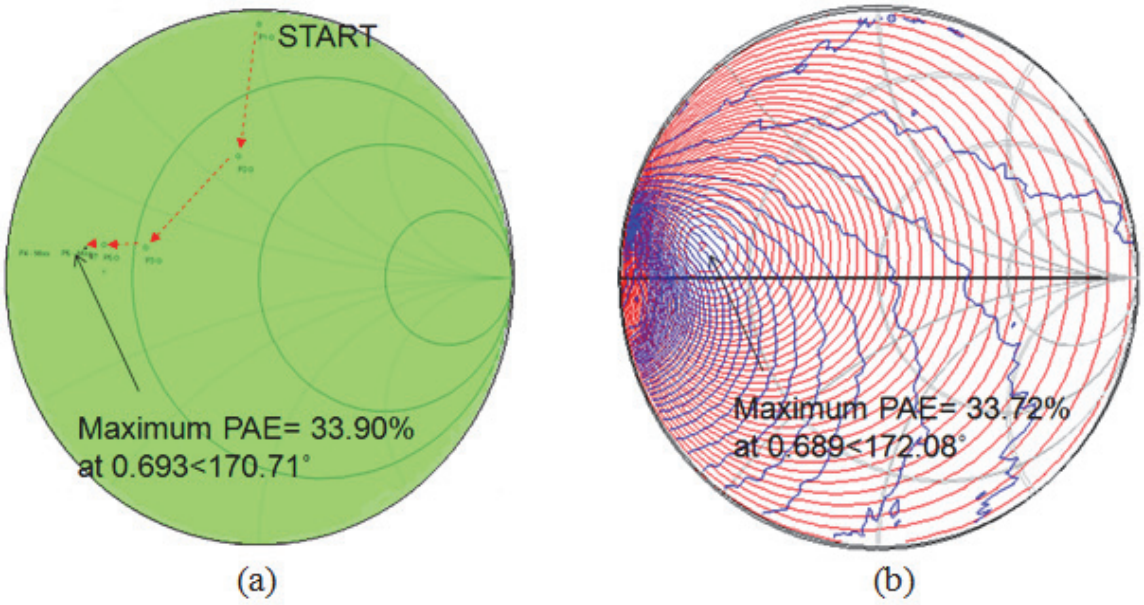

Figure 6.2: (a) Steepest Ascent Algorithm for PAE and (b) Simulated PAE Location on Smith Chart

The factors D_n and D_s were noted in Chapter 5 to affect the number of measurements required for convergence, as well as the resolution of the search. The algorithm takes three measurements for each candidate point in order to determine the gradient in a neighborhood around the candidate point. A step D_s is taken in the direction

of the gradient in order to approach the optimum of either PAE or ACPR. The D_n chosen for this test, in terms of |Γ|, is 0.05, and the D_s starts at 0.5. The algorithm proceeds from point to point as shown in Figure 6.2a until reaching the PAE optimum. One of the key performance features of this algorithm is the number of measurements required to converge on the optimum objective location. The locations marked by a circle in Figure 6.2a indicate candidate points which resulted in three measurements. Candidate points which demonstrate a decline in PAE only require one measurement, and the search returns to the previous candidate after this is ascertained. The single PAE steepest ascent required 18 total measurements before reaching the objective peak value. The PAE value approximated by a final parabola fit is shown to be within 0.18% of the load-pull simulation maximum at approximately the same location. The vector distance |Γ| on the Smith chart between the complete load-pull optimum PAE location and the search PAE optimum is approximately 0.0170 units, which is less than D_n and within the search resolution. This difference indicates that the accuracy of the algorithm for predicting the magnitude at the PAE peak location.

The steepest descent algorithm for ACPR begins at the PAE optimum location as described in Chapters 4 and 5, and is shown in Figure 6.3a. The neighboring point distance remains the same as that for PAE, but D_s is reduced to equal D_n. This reduction is due to the fact that the affine approximation of the Pareto curve using steepest descent depends on a small D_s for the ACPR search. Reducing D_s, however, also increases the number of measurements required to reach the ACPR optimum. The steepest descent algorithm for ACPR reaches its optimum load reflection coefficient at approximately $0.935\angle -173.43^{o}$. The vector distance between the ACPR optimum predicted by the complete load-pull and that of the search algorithm is 0.0578 units, with a magnitude

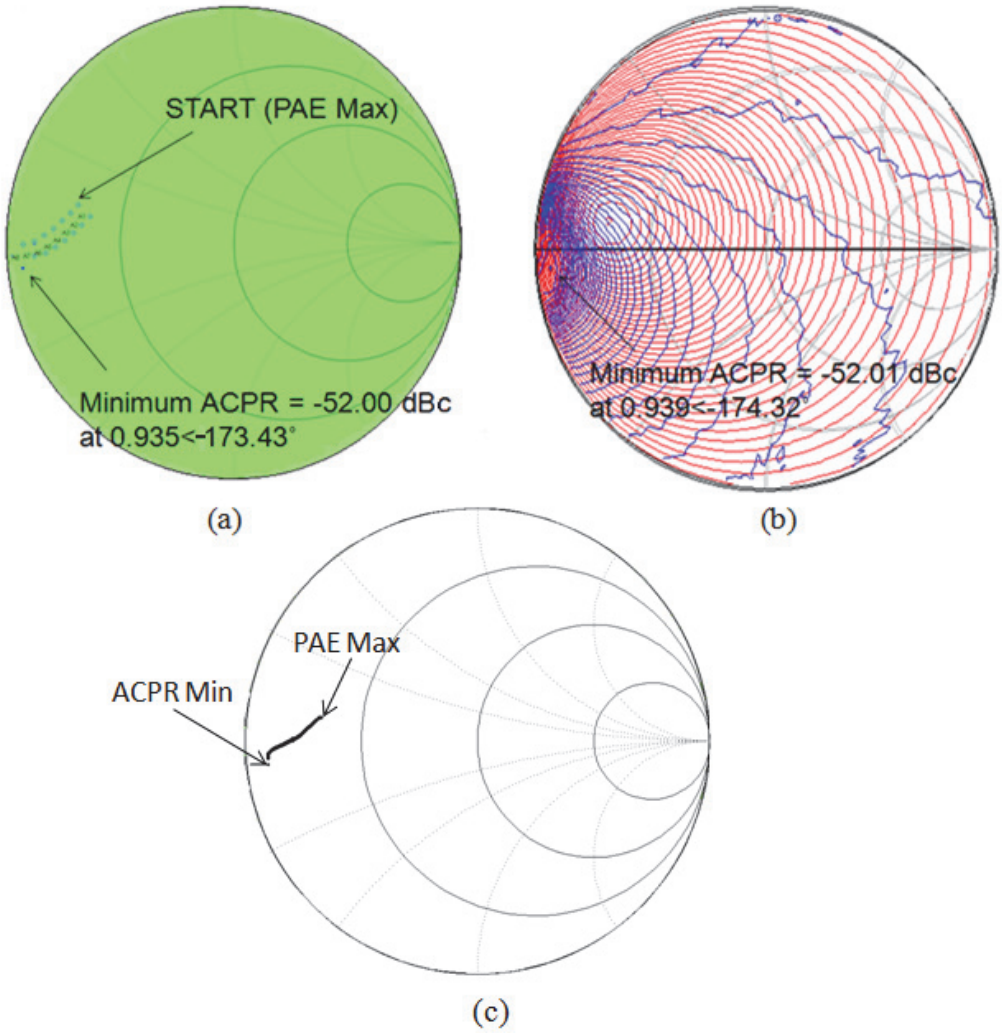

Figure 6.3: (a) Steepest Descent Algorithm for ACPR, (b) Simulated ACPR Location on Smith Chart, and (c) Pareto Path Between PAE and ACPR

difference of 0.0176 dBc. The Pareto curve path is approximated by the small step-size ACPR steepest descent in Figure 6.3c. The algorithm seems to closely approximate the Pareto curve between PAE and ACPR.

To demonstrate the robustness of the peak search algorithm, multiple instantiations were performed from six initial points as shown in Figure 6.4. The red arrows show the approximate paths of the PAE steepest ascent. Each PAE path follows a slightly different trajectory which is dependent upon the location, but all converge in a

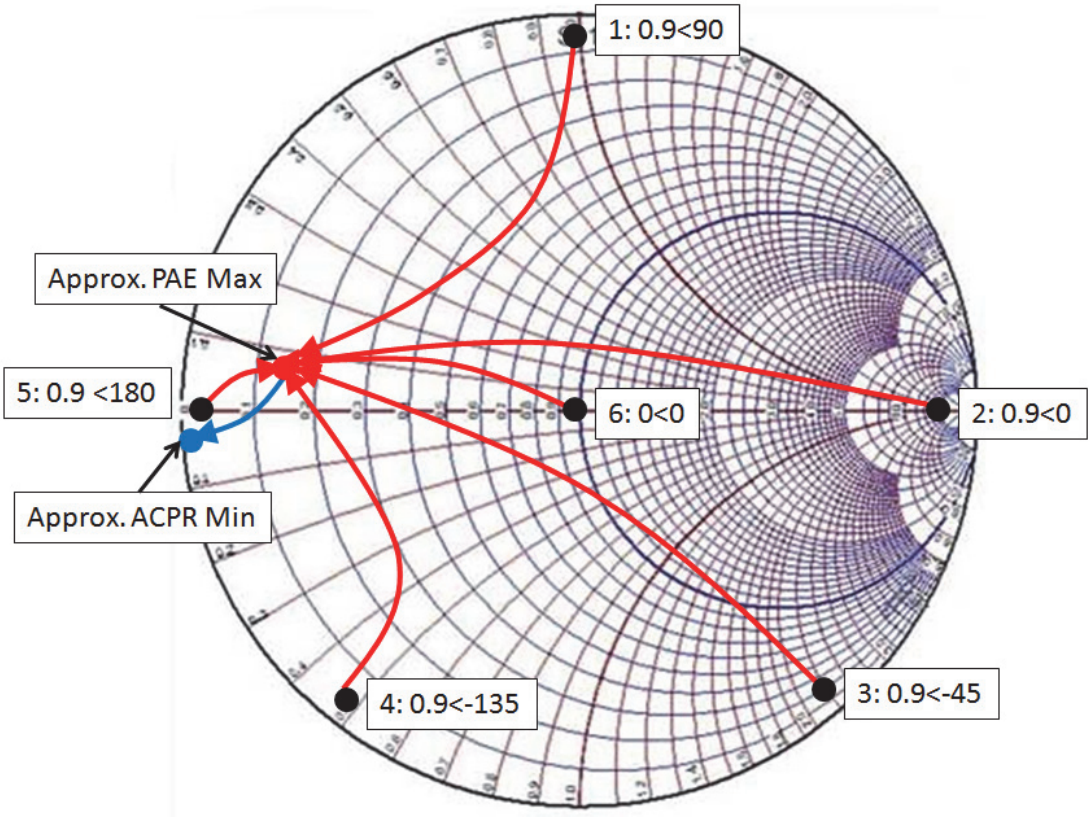

Figure 6.4: Sequential peak search Simulation Initializations and Approximate Paths for PAE (red) and ACPR (blue)

small region around the simulated PAE optimum. The arrow shown in blue indicates the approximate path for the ACPR searches. These ACPR paths are relatively the same for each search due to the precision of the PAE search for the six instantiations. The data shown in Table 6.2 shows the convergence point of the PAE steepest ascent routine. Absolute error is used to show the difference in magnitude between the maximum found by the complete simulated load-pull and give a convergence metric for each instantiation. The number of measurements is also shown in this table and directly influences the convergence time for the algorithm.

Table 6.2: Simulation PAE Instantiation Data with $D_n = 0.05$ and $D_s = 0.5$

Start	Magnitude	Angle	Resistance (Ω)	Reactance (Ω)	PAE Value	Absolute Error	Number of Measurements to Finish
1	0.6932906	170.7008	0.182290705	0.07864404	33.90044	0.173369	18
2	0.6751853	170.6682	0.195140484	0.07852769	33.84273	0.115659	20
3	0.6781347	170.8636	0.192978557	0.07694217	33.84127	0.114199	17
4	0.6767859	170.6321	0.194003719	0.07886901	33.88235	0.155279	21
5	0.6768629	170.6631	0.193940359	0.07860872	33.88946	0.162389	27
6	0.674366	170.7021	0.195719055	0.07822274	33.85939	0.132319	15

The standard deviations and mean of the PAE steepest ascent algorithm are shown in Table 6.3. The difference between the mean value and the optimum PAE point on the complete load-pull simulation is 0.1497%, which is small compared to the magnitude of the dataset. The low standard deviation values for impedance and magnitude indicate that the measurement is repeatable and can achieve high precision from arbitrary starting locations.

Table 6.3: Mean and Standard Deviation for Simulation PAE Searches

Dataset	Resistance (Ω)	Reactance (Ω)	PAE Value
Mean:	0.19234548	0.0783024	33.86927333
Standard Deviation:	0.005019676	0.00069841	0.025045069

Table 6.4 shows the second portion of the algorithm in which the ACPR objective is reached. A distinguishing characteristic of the PAE and ACPR search routines is the number of measurements required for convergence. The ACPR dataset requires a significant increase in the number of measurements due to the constraint on D_s. The absolute error indicates that the ACPR converge point is close to the optimum predicted through the load-pull simulation. Table 6.5 indicates that the mean value of the instantiations is close to the simulated optimum value of -52.01 dBc.

Table 6.4: Simulation ACPR Instantiation Data with $D_n = 0.05$ and $D_s = 0.05$

Start	Magnitude	Angle	Resistance(Ω)	Reactance(Ω)	ACPR Value	Absolute Error (dB)	Number of Measurements to Finish
1	0.9352575	-173.4321	0.033564222	-0.0573142	-51.99625	0.017563	25
2	0.9470977	-174.1006	0.027241908	-0.0514894	-51.99362	0.020193	27
3	0.9470163	-173.1394	0.027310469	-0.0598971	-51.95176	0.062053	31
4	0.9474341	-172.6199	0.027104577	-0.0644455	-52.06803	0.054217	33
5	0.9471099	-172.5858	0.027277333	-0.0647435	-52.06282	0.049007	33
6	0.9469489	-174.1005	0.027320622	-0.05149	-51.99499	0.018823	28

The magnitude difference between these two numbers is 0.11245, which is small compared to the size of the datasets. The sequential peak search for PAE and ACPR has been demonstrated using an ADS software simulation for a wideband modulated signal. The next step is to verify the test results for an adaptive load-pull test bench for radar chirp signals.

Table 6.5: Mean and Standard Deviation for the Simulation ACPR Searches

Dataset	Resistance(Ω)	Reactance(Ω)	ACPR Value
Mean:	0.028303189	-0.05823	-52.011245
Standard Deviation:	0.002578556	0.00592521	0.045216585

6.2 Sequential Peak Search Algorithm Using Load-Pull Test Bench

The results from our new optimization were compared to traditionally measured PAE and ACPR load-pull results, as shown in Figure 6.5a. The DUT for this measurement is the Skyworks SKY65017-70LF InGaP amplifier, which reaches approximately 2dB compression with a 50 ohm load termination at an input power of 2 dBm used. The optimum values and locations for PAE and ACPR optimum points are shown in Table 6.6. The excitation is a linear frequency modulated chirp which spans 16 MHz and has a repetition rate of 62.5 microseconds with 100% duty cycle. Figure 6.5b

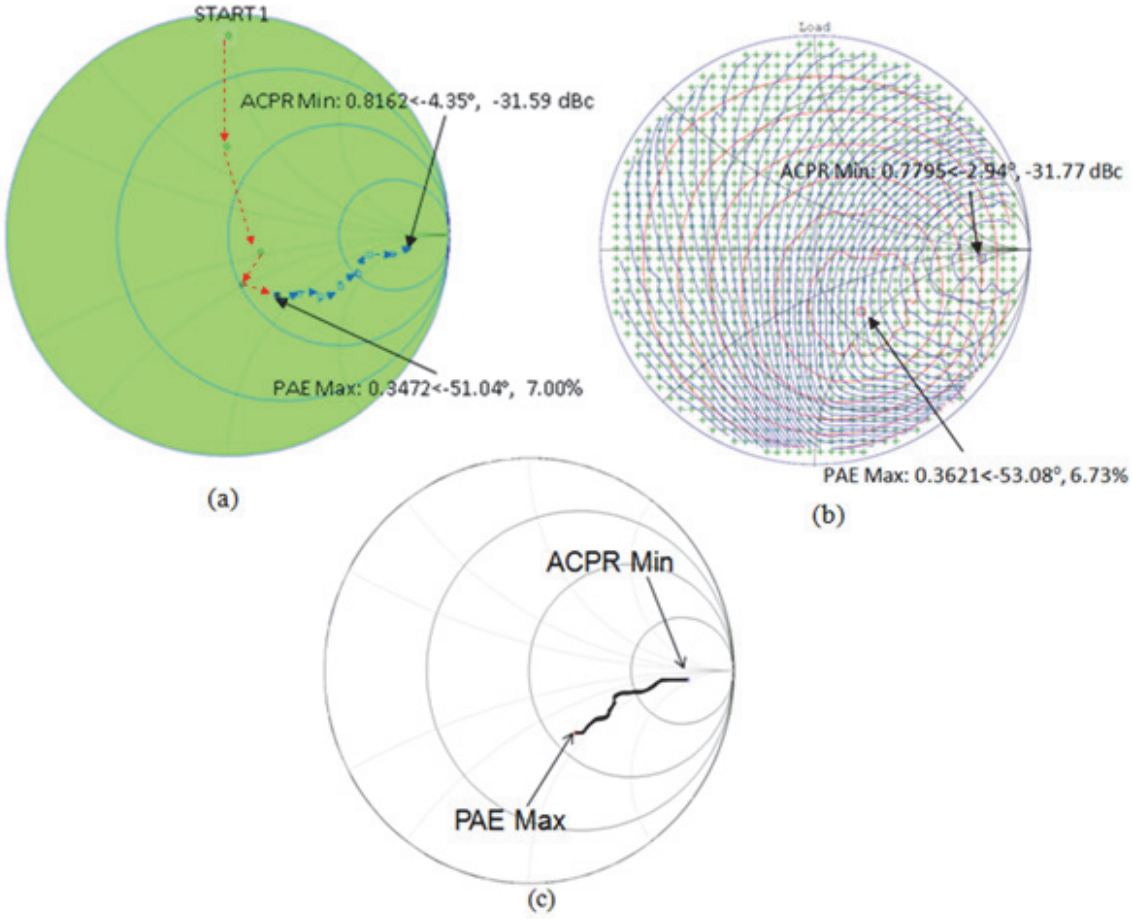

Figure 6.5: (a) Measurement-Based Peak Search Algorithm for PAE and ACPR, (b) Measured PAE and ACPR Locations on Smith Chart, and (c) Pareto Path Between PAE and ACPR

shows traditional load-pull results for PAE and ACPR, which required 1178 impedances to be measured to generate contours for PAE and ACPR. Following the identification of the maximum PAE point, a steepest descent with a very small search distance was used to guide the measurement toward the ACPR minimum.

Figure 6.5a shows results for the bi-objective steepest-ascent algorithm starting from a reflection coefficient of $0.9\angle 90^{o}$, which reaches the maximum PAE point in 21 measurements. The value of the predicted PAE maximum deviates by 0.27% as from the standard peak in Table 6.6. The difference in rectangular distance between the predicted

Table 6.6: Measurement Load-Pull Data Standard

Data	Magnitude	Angle	Resistance (Ω)	Reactance (Ω)	Value
PAE	0.3621	-53.08	1.24823464	-0.831760046	6.73
ACPR	0.7795	-2.94	7.74348901	-1.578012047	-31.77

PAE optimum location and that of the complete load-pull is approximately 0.0195 units, which is smaller than D_n and within the resolution of the search. An important feature to note is the apparent flatness that occurs near the peak of the PAE objective function as indicated by the contours in 6.5b. The large neighborhood of points surrounding the PAE maximum location, which have values near that of the PAE maximum, can cause the algorithm to converge onto a point near the maximum. This minor deviation is due to the limited resolution of the search, which interprets the region surrounding the PAE peak to be flat. Under these considerations predicted value resides reasonably close to the true PAE maximum predicted by the load-pull in Figure 6.5b.

The ACPR steepest descent begins at the location of the PAE maximum and reaches its minimum in 25 measurements. The measured ACPR search differs from that of the simulated ACPR search in that a larger D_n of 0.1 is used instead of 0.05. A larger value is chosen to make the gradient calculation for ACPR less dependent on fluctuations in the measurement. The ACPR algorithm differed in location by a rectangular distance of 0.0416. The ACPR minimum appears to be found at a location very close to the true minimum and varies in magnitude by 0.18 dBc. Figure 6.5c shows the Pareto path calculated from the load-pull data. Because the piecewise affine approximation of the Pareto curve is performed (by necessity) using backward difference, a "lag" appears to be introduced when comparing the Pareto curve to the ACPR steepest descent path in Figure 6.5b. It appears that the slope of the affine approximation lags behind slope changes in

the actual Pareto curve. A larger D_s and D_n for the measurement of ACPR gradients also seems to introduce error in the Pareto trace by steepest descent. This is expected due to the explanation of affine approximation in Chapter 4, where the Pareto curve cannot be guaranteed for sizeable steps. The ACPR steepest descent, however, appears to reasonably approximate the Pareto curve and traces similar path features.

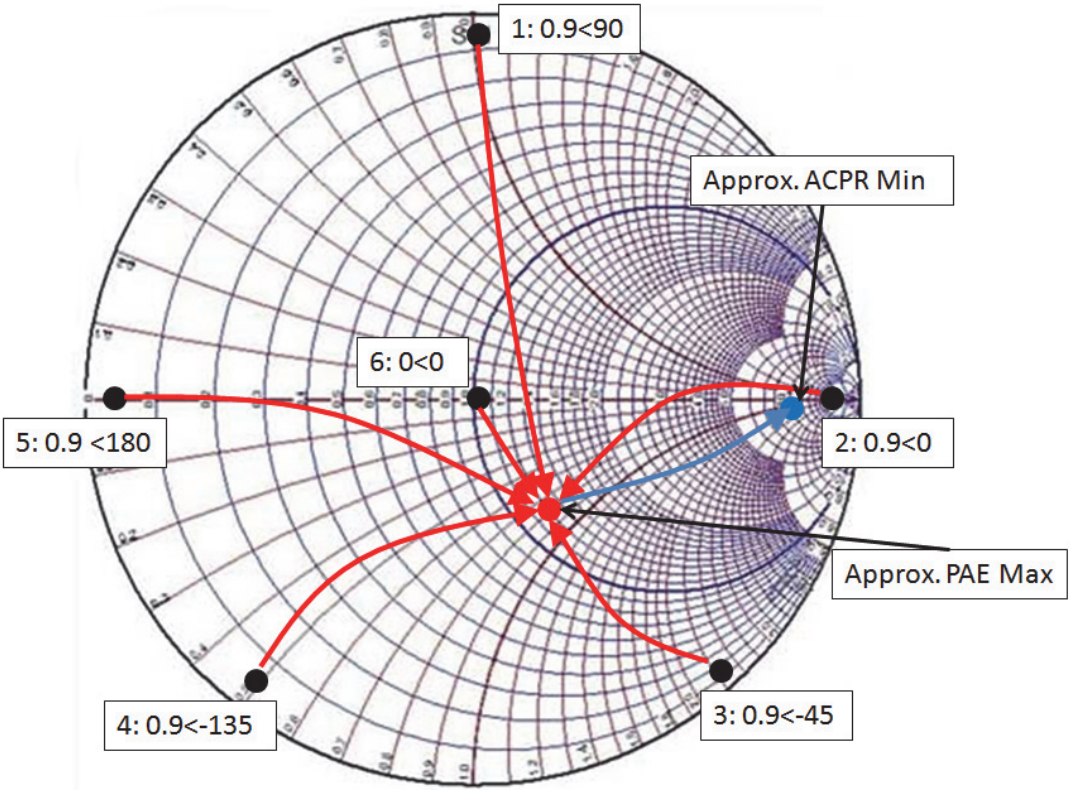

Figure 6.6: Measurement Sequential peak search Simulation Initializations and Approximate Paths for PAE (red) and ACPR (blue)

Figure 6.6 shows the search is robust regardless of the search starting point. The paths for convergence from each of the initial six starting locations approximately converge to the PAE maximum and ACPR minimum. Tables 6.7 and 6.8 show the data for the six PAE instantiations. The number of measurements used in the PAE steepest ascent searches is shown to not depend solely on measurement locations. Start location

5, for example, has a significant increase in measurements due to stepping over the peak but continually landing on a surface of greater magnitude than the previous. Another example is the start location 3, except this case shows a quicker convergence due to a coincidental advantage of D_s and PAE surface. The PAE standard deviation is significant when compared to the location of the PAE peak, but these differences are due to flatness around the maximum as previously stated. The difference between the mean and optimum PAE peak measured by load-pull is 0.004421 and indicates that the algorithm is predicting an accurate PAE value consistently.

Table 6.7: Measurement PAE Instantiation Data with $D_n = 0.05$ and $D_s = 0.5$

Start	Magnitude	Angle	Resistance (Ω)	Reactance (Ω)	PAE Value	Absolute Error	Number of Measurements to Finish
1	0.252288	-53.93013	1.22148217	-0.532044	6.746166	0.016166	21
2	0.3739062	-31.38345	1.715593358	-0.7766953	6.785289	0.055289	18
3	0.2849819	-50.49038	1.278578109	-0.6119366	6.898914	0.168914	12
4	0.3579688	-41.67054	1.469381648	-0.8022046	6.672305	0.057695	15
5	0.2899597	-70.099741	1.032979052	-0.614979	6.732541	0.002541	27
6	0.4938317	-55.76996	1.098559708	-1.1863942	6.571313	0.158687	21

Table 6.8: Mean and Standard Deviation for Measurement PAE Searches

Dataset	Resistance (Ω)	Reactance (Ω)	PAE Value
Mean:	1.302762341	-0.7540423	6.734421333
Standard Deviation:	0.252928655	0.23604102	0.109772125

Tables 6.9 and 6.10 show the second half of the sequential peak search algorithm for ACPR. The standard deviation of the ACPR locations shows significant variation, but is likely due to the standard deviation of the starting PAE maximum locations. Recall the flatness near the PAE maximum point, which causes the algorithm to converge onto maximum points surrounding the true maximum. From the theory in Chapter 4, the

Pareto front can only be approximated by the steepest descent algorithm if the starting location is a Pareto point. Since there is some variation in these starting locations, those path which do not begin exactly on the PAE maximum will also cause the steepest descent approximation of the Pareto front to vary from the true Pareto front. Given that that ACPR starting locations are not precise, some variation is expected in predicted ACPR optimum location. The absolute error in Table 6.9, however, shows the APCR magnitude to be very close to the measured load-pull minimum. The difference between the mean ACPR and the actual minimum measured by traditional load-pull is about 0.007713.

Table 6.9: Measurement ACPR Instantiation Data with $D_n = 0.1$ and $D_s = 0.1$

Start	Magnitude	Angle	Resistance(Ω)	Reactance(Ω)	ACPR Value	Absolute Error (dB)	Number of Measurements to Finish
1	0.8169921	-0.8808125	9.871581355	-0.745685	-31.8342	0.0642	25
2	0.6898305	-3.387087	5.314942597	-0.8265697	-31.712	0.058	25
3	0.8342393	-4.892497	9.060883278	-4.2406618	-31.81052	0.04052	22
4	0.7847384	-2.151674	8.097642801	-1.2420073	-31.74476	0.02524	21
5	0.815112	-4.792841	8.414219154	-3.4151731	-31.80691	0.03691	18
6	0.9133468	-4.507479	12.59995602	-10.909867	-31.75438	0.01562	25

The standard deviation is also three orders of magnitude lower than the ACPR optimum magnitude. These two calculations show the magnitude of the ACPR optimum being accurately predicted by the sequential peak search algorithm.

Table 6.10: Mean and Standard Deviation for Measurement ACPR Searches

Dataset	Resistance(Ω)	Reactance(Ω)	ACPR Value
Mean:	8.8932042	-3.5633273	-31.77712833
Standard Deviation:	2.382924585	3.87994461	0.047044706

6.3 Conclusion

The results of the sequential peak search algorithm have been shown for various instantiations for both simulation and measurement instantiations. These tests have been shown to converge on the PAE and ACPR optimum locations predicated by simulated and measured load-pull to a high degree of precision. Additionally, the ACPR steepest descent algorithm closely approximates the Pareto tradeoff curve between PAE and ACPR for both simulated and measured data. The next chapter will discuss possible applications and improvements to the current algorithm.

CHAPTER SEVEN

Conclusion

A method for optimizing the performance characteristics of adaptive radar transmitters has been shown through the design of an algorithm which shows promise for use in reconfigurable impedance tuning. These techniques are expected to enable automatic adjustment of transmitter amplifier performance for PAE and ACPR to further extend the detection capabilities of radar systems under spectral mask constraints. The intelligent optimization algorithm unifies two gradient-based searches for PAE and ACPR to produce an optimal tradeoff curve between the two objectives. Solutions along the Pareto curve correspond to impedances which yield a weighted tradeoff between two objectives. The results for simulation and measurement implementations indicate that the combined steepest ascent algorithm closely approximates the Pareto tradeoff curve between PAE and ACPR.

There are a few limitations to using the combined steepest ascent algorithm, one of them being that only unimodal objectives are considered. Multimodal objective functions would exhibit local minima which can cause the steepest ascent algorithm to convergence on a local minimum instead of the global maximum [47]. The optimization routine assumes that the contours for both PAE and ACPR functions are unimodal. Another potential source of error comes from the fact that an affine approximation of the Pareto curve can accumulate significant error for successive steepest descent iterations. This error occurs because each step overshoots a number of points which have different gradients, indicating that the new point will be off of the Pareto optimum curve. Since

the new step will be made at a point where the gradients are not are not collinear, the algorithm may miss the next point along the Pareto path. Although the ACPR optimum point will still be located under the unimodal case, the error between the actual trace and the actual Pareto curve increases as the measurement continues.

Potential improvements upon this work would include increasing the accuracy of the Pareto tracing by redirecting the algorithm back towards the Pareto curve between PAE and ACPR. This modification would reduce the error accumulated between measurements and provide a more accurate trace of the Pareto optimal solutions. Utilizing information provided by the gradients for PAE and ACPR points, a "nudge factor" would adjust the steepest descent for ACPR so that it follow the Pareto optimal path. An even better modification is a method for quickly converging onto a desired Pareto optimum point for a fixed ACPR maximum, finding the Pareto optimum without first searching for the maximum PAE reflection coefficient. There may be applications in which the entire Pareto curve between PAE and ACPR is not needed. A single search could allow decreased time to convergence on the solution. A fast Pareto convergence algorithm may use information about the gradients taken at a candidate point to roughly estimate the distance from a Pareto optimal point.

The real-time Pareto tracing of the combined steepest ascent algorithm has a few important ramifications for adaptive radar systems. Implementing automated impedance tuners as part of the transmitter amplifier provides a means to partially redesign the amplifier for certain applications. This could be desirable for radar systems which must adapt to a continually changing electromagnetic environment, such as those which are utilized around the world under varying spectral constraints. Adaptive radar with such flexibility can maximize detection when the spectral constraints are relaxed, and reduce

emissions when those constraints are increased. Additionally, the affine approximation of the Pareto curve between PAE and ACPR allows for the efficiency to be maximized for constraints on the output emission. This feature provides an alternative to power back-off of the transmitter, which may sacrifice more performance than is needed to meet the spectral mask. There is immense potential for including the algorithm into a larger optimization scheme for waveforms due to the fact that the impedance tuning is driven by software. Optimized radar waveforms such as continuous phase modulation [63] can be generated using software and arbitrary waveform generators. Such a system may be augmented by modifying the waveform and amplifier output impedance simultaneously to further enhance the detection capacities of radar systems with spectrum constraints. Lastly, the use of automated impedance tuning adjusts fundamental parameters in amplifier design without modifications to circuit topology, and may be a more simple way to negotiate the tradeoff between linearity and efficiency for power amplifiers under different modulated signal excitations.

BIBLIOGRAPHY

[1] Ahmad, F.; Amin, M.G.; , "Radar waveform design for detection of weapons," *Cognitive Information Processing (CIP), 2010 2nd International Workshop on* , vol., no., pp.258-262, 14-16 June 2010.

[2] Wei, Yimin; Meng, Huadong; Liu, Yimin; Wang, Xiqin; , "Radar phase-modulated waveform design for extended target detection," *Tsinghua Science and Technology* , vol.16, no.4, pp.364-370, Aug. 2011.

[3] Junliang Qu; Xu Jia; Yingning Peng; Xiutan Wang; , "Optimal waveform design for MIMO radar detection with clutter and noise," *Radar (Radar), 2011 IEEE CIE International Conference on* , vol.1, no., pp.559-563, 24-27 Oct. 2011.

[4] Jeongwoo Han; Cam Nguyen; , "A multi-band UWB radar for sensing objects," *Antennas and Propagation Society International Symposium, 2007 IEEE* , vol., no., pp.4917-4920, 9-15 June 2007.

[5] Feng Zhou; Tong Xu; , "High resolution methods for electronic counter measures environments establishing and side lobe cancellation in cognitive radar," *Intelligent Computing and Intelligent Systems (ICIS), 2010 IEEE International Conference on* vol.2, no., pp.805-808, 29-31 Oct. 2010.

[6] Guerci, J.R.; , "Cognitive radar: A knowledge-aided fully adaptive approach," *Radar Conference, 2010 IEEE* , vol., no., pp.1365-1370, 10-14 May 2010.

[7] Chun-Yang Chen; Vaidyanathan, P.P.; , "MIMO Radar Ambiguity Properties and Optimization Using Frequency-Hopping Waveforms," *Signal Processing, IEEE Transactions on* , vol.56, no.12, pp.5926-5936, Dec. 2008.

[8] Luo, Mei-fang; Kong, Ling-jiang; Cui, Guo-long; , "A sidelobe suppression method based on adaptive pulse compression (apc) for random stepped-frequency radar," *Radar Conference, 2009 IET International* , vol., no., pp.1-4, 20-22 April 2009.

[9] Baylis, C.; Wang, L.; Moldovan, M.; Martin, J.; Miller, H.; Cohen, L.; de Graaf, J.; , "Designing transmitters for spectral conformity: power amplifier design issues and strategies," *Radar, Sonar & Navigation, IET* , vol.5, no.6, pp.681-685, July 2011.

[10] Wang, L.S.; McGeehan, J.P.; Williams, C.; Doufexi, A.; , "Application of cooperative sensing in radar-communications coexistence," *Communications, IET* vol.2, no.6, pp.856-868, July 2008.

[11] J. de Graaf, H. Faust, J. Alatishe, and S. Talapatra, “Generation of Spectrally Confined Transmitted Radar Waveforms,” Proceedings of the IEEE Conference on Radar, 2006, pp. 76-83.

[12] “Broadband Plan”: http://www.broadband.gov.

[13] Seung-June Yi; Sangwook Nam; Sung-Hoon Oh; Jae-Hee Han; , "Prediction of a CDMA output spectrum based on intermodulation products of two-tone test," *Microwave Theory and Techniques, IEEE Transactions on* , vol.49, no.5, pp.938-946, May 2001.

[14] S. Cripps, *RF Power Amplifiers for Wireless Communications*. Norwood, Maine: Artech House, 2006.

[15] Z Wang, M Ganley, Bal Randhawa, I Parker,“Interference from Radars into Adjacent Band UMTS and WiMAX Systems”, ERA Tech.,Surrey,UK, Rep. 2007-0554, 2007.

[16] M. Richards, J. Scheer, W. Holm, “*Fundamentals of Pulse Compression Waveforms*,” in *Principles of Modern Radar: Basic Principles*,Raleigh,NC: SciTech, 2010, pp.774.

[17] Sevic, J.F.; Steer, M.B.; Pavio, A.M.; , "Large-signal automated load-pull of adjacent-channel power for digital wireless communication systems," *Microwave Symposium Digest, 1996., IEEE MTT-S International* , vol.2, no., pp.763-766 vol.2, 17-21 Jun 1996.

[18] Sevic, J.F.; Staudinger, J.; , "Simulation of power amplifier adjacent-channel power ratio for digital wireless communication systems," *Vehicular Technology Conference, 1997, IEEE 47th* , vol.2, no., pp.681-685 vol.2, 4-7 May 1997.

[19] Hsin-Chin Chang; Seng-Woon Chen; Moe, D.; Hackman, S.; , "CDMA ACPR prediction using two-tone intermodulation spectrum by modeling device non-linearity with Tchebyshev polynomials," *Wireless Communications Conference, 1997., Proceedings* , vol., no., pp.117-120, 11-13 Aug 1997.

[20] Jonggyun Lim; Wonshil Kang; Hyunchul Ku; , "Compensation of path imbalance in LINC transmitters using EVM and ACPR look up tables," *Microwave Conference Proceedings (APMC), 2010 Asia-Pacific* , vol., no., pp.1296-1299, 7-10 Dec. 2010.

[21] Svensson, T.; Eriksson, T.; , "On Power Amplifier Efficiency with Modulated Signals," *Vehicular Technology Conference (VTC 2010-Spring), 2010 IEEE 71st* , vol., no., pp.1-5, 16-19 May 2010.

[22] Darraji, R.; Ghannouchi, F.M.; Hammi, O.; , "Generic loadpull- based design methodology for performance optimization of doherty amplifiers," *Science, Measurement & Technology, IET* , vol.6, no.3, pp.132-138, May 2012.

[23] Hammi, O.; Sirois, J.; Boumaiza, S.; Ghannouchi, F.M.; ,"Design and performance analysis of mismatched Doherty amplifiers using an accurate load-pull-based model,"*Microwave Theory and Techniques, IEEE Transactions on*, vol.54, no.8, pp.3246-3254, Aug. 2006.

[24] Sirois, J.; Boumaiza, S.; Helaoui, M.; Brassard, G.; Ghannouchi, F.M.; , "A robust modeling and design approach for dynamically loaded and digitally linearized Doherty amplifiers," *Microwave Theory and Techniques, IEEE Transactions on* , vol.53, no.9, pp. 2875- 2883, Sept. 2005.

[25] Ubostad, M.; Olavsbraten, M.; , "Linearity performance of an RF power amplifier under different bias-and load conditions with and without DPD," *Radio and Wireless Symposium (RWS), 2010 IEEE* , vol., no., pp.232-235, 10-14 Jan. 2010.

[26] Baylis, C.; Wang, L.; Moldovan, M.; Martin, J.; Miller, H.; Cohen, L.; de Graaf, J.; , "Designing transmitters for spectral conformity: power amplifier design issues and strategies,"*Radar, Sonar & Navigation, IET* , vol.5, no.6, pp.681-685, July 2011.

[27] Besombes, F.; Mazeau, J.; Martinaud, J.P.; Mancuso, Y.; Sommet, R.; Mons, S.; Ngoya, E.; , "Electro-thermal behavioral modeling of RF power amplifier taking into account load-pull effects for narrow band radar applications," *Microwave Integrated Circuits Conference (EuMIC), 2011 European* , vol., no., pp.264-267, 10-11 Oct. 2011.

[28] Martin, J.; Moldovan, M.; Baylis, C.; Marks, R.J.; Cohen, L.; de Graaf, J.; , "Radar chirp waveform selection and circuit optimization using ACPR load-pull measurements," *Wireless and Microwave Technology Conference (WAMICON), 2012 IEEE 13th Annual* , vol., no., pp.1-4, 15-17 April 2012.

[29] Joongjin Nam; Bumman Kim; , "The Doherty Power Amplifier With On-Chip Dynamic Bias Control Circuit for Handset Application," *Microwave Theory and Techniques, IEEE Transactions on* , vol.55, no.4, pp.633-642, April 2007.

[30] Wei-Chun Hua; Hung-Hui Lai; Po-Tsung Lin; Chee Wee Liu; Tzu-Yi Yang; Gin-Kou Ma; , "High-linearity and temperature-insensitive 2.4 GHz SiGe power amplifier with dynamic-bias control," *Radio Frequency integrated Circuits (RFIC) Symposium, 2005. Digest of Papers. 2005 IEEE* , vol., no., pp. 609- 612, 12-14 June 2005.

[31] Staudinger, J.; Gilsdorf, B.; Newman, D.; Norris, G.; Sadowniczak, G.; Sherman, R.; Quach, T.; Wang, V.; , "800 MHz power amplifier using envelope following technique," *Radio and Wireless Conference, 1999. RAWCON 99. 1999 IEEE* , vol., no., pp.301-304, 1999.

[32] Je-Kuan Jau; Yu-An Chen; Tzyy-Sheng Horng; Jian-Yu Li; , "Envelope Following-Based RF Transmitters Using Switching-Mode Power Amplifiers," *Microwave and Wireless Components Letters, IEEE* , vol.16, no.8, pp.476-478, Aug. 2006.

[33] Hassan, M.; Myoungbo Kwak; Leung, V.W.; Chin Hsia; Yan, J.J.; Kimball, D.F.; Larson, L.E.; Asbeck, P.M.; , "High efficiency envelope tracking power amplifier with very low quiescent power for 20 MHz LTE," *Radio Frequency Integrated Circuits Symposium (RFIC), 2011 IEEE* , vol., no., pp.1-4, 5-7 June 2011.

[34] Hassan, M.; Larson, L.E.; Leung, V.W.; Kimball, D.F.; Asbeck, P.M.; , "A Wideband CMOS/GaAs HBT Envelope Tracking Power Amplifier for 4G LTE Mobile Terminal Applications," *Microwave Theory and Techniques, IEEE Transactions on* , vol.60, no.5, pp.1321-1330, May 2012.

[35] Li, C.-J.; Chen, C.-T.; Horng, T.-S.; Jau, J.-K.; Li, J.-Y.; Deng, D.-S.; , "Hybrid quadrature polar modulator-based transmitter with digital predistorter for simultaneous enhancement of adjacent channel power ratios and power added efficiency (PAE)," *Microwaves, Antennas & Propagation, IET* , vol.2, no.8, pp.801-812, December 2008.

[36] Baylis, C.; Moldovan, M.; Wang, L.; Martin, J.; , "LINC power amplifiers for reducing out-of-band spectral re-growth: A comparative study," *Wireless and Microwave Technology Conference (WAMICON), 2010 IEEE 11th Annual* , vol., no., pp.1-4, 12-13 April 2010.

[37] Ghannouchi, F.M.; Hashmi, M.S.;,"Load-pull techniques and their applications in power amplifiers design (invited)," *Bipolar/BiCMOS Circuits and Technology Meeting (BCTM), 2011 IEEE* , vol., no., pp.133-137, 9-11 Oct. 2011.

[38] Patil, P.; Varanasi, R.; Dunleavy, L.P.; , "On triplexers and their applications to harmonic load-pull," *ARFTG Microwave Measurements Conference, 2003. Fall 2003. 62nd* , vol., no., pp. 215- 225, 4-5 Dec. 2003.

[39] Hoversten, J.; Roberg, M.; Popović, Z.; , "Harmonic load pull of high-power microwave devices using fundamental-only load pull tuners," *Microwave Measurements Conference (ARFTG), 2010 75th ARFTG* , vol., no., pp.1-4, 28-28 May 2010.

[40] Ebrahimi, M.M.; Helaoui, M.; Ghannouchi, F.M.; , "Minimizing matching network loss in output harmonic matched power amplifiers using harmonic load-pull measurement," *Power Amplifiers for Wireless and Radio Applications (PAWR), 2012 IEEE Topical Conference on* , vol., no., pp.61-64, 15-18 Jan. 2012.

[41] Gonzales, G. *Microwave Transistor Amplifiers*. Upper Saddle River, New Jersey: Prentice Hall, 1997, pp. 308.

[42] L,A, Geis, L.P. Dunleavy, “Power Contour Plots Using Linear Simulator”. Microwave J., Vol. 39, N.6. June 1996, pp. 60-70.

[43] J. B. Call, "Large-Signal Characterization and Modeling of Non-Linear Devices Using Scattering Parameters," M. Sc. Thesis, Virginia Polytechnic Institute, Sept. 2002, Chapter 4, pp. 97-110.

[44] Patterson, Howard; Scarpitto, Forrest; Bielick, Brian; , "Broadband Characterization of GaN Transistors for Software Defined Radio Power Amplifier Applications," *Military Communications Conference, 2007. MILCOM 2007. IEEE* , vol., no., pp.1-7, 29-31 Oct. 2007.

[45] Zadeh LA. Fuzzy Sets. *Information and Control*. University of California, California 1965; 8: 338-353.

[46] Bloch E., *A First Course in Geometric Topology and Differential Geometry*, Boston, Birkhauser, pg.111, 1997.

[47] Boyd S., Vandenberghe L., *Convex Optimization*. New York, Cambridge Press, 2004.

[48] Indraneel Das and J. E. Dennis. Normal-Boundary Intersection: A New Method for Generating the Pareto Surface in Nonlinear Multicriteria Optimization Problems. *SIAM J. on Optimization*, 631-657, March 1998.

[49] Il Yong Kim and Olivier de Weck.“Adaptive weighted sum method for multiobjective optimization: a new method for Pareto front generation”, Structural and Multidisciplinary Optimization, Vol. 31, pp. 105-116, 2006.

[50] Emmerich, M., and A. Deutz. Multicriteria Optimization and DecisionMaking. LIACS . Leiden university, NL. 2006.

[51] Angelopoulos, S., Order-preserving Transformations and Greedy-like Algorithms.*WAOA*, pp. 197-210, 2004.

[52] Lovison, A.: Singular continuation: Generating Piecewise Linear Approximations to Pareto Sets via Global Analysis. SIAM J. Optim. 21(2), 463–490 (2011).

[53] D. Qiao, R. Molfino, S. Lardizabal, B. Pillans, P. Asbeck, andG. Jerinic, “An Intelligently Controlled RF Power Amplifier with a Reconfigurable MEMS-Varactor Tuner,” IEEE Trans. on Microwave Theory and Techniques, Vol.53, No.3, Part 2, pp. 1089-1095, March 2005.

[54] C. Baylis, L. Dunleavy, S. Lardizabal, R. J. Marks II, and A. Rodriguez, “Efficient Optimization Using Experimental Queries: A Peak-Search Algorithm for Efficient Load-Pull Measurements,” *Journal of Advanced Computational Intelligence and Intelligent Informatics,* Vol.15, pp. 13-20, 2011.

[55] A.P. de Hek, "A Novel Fast Search Algorithm for an Active Load-Pull Measurement System," GaAs Symposium, Amsterdam, The Netherlands, 1998.

[56] S. Perlow, “New Algorithms for the Automated Microwave Tuner Test System,” RCA Review, Vol.46, pp. 341-355, September 1985.

[57] Blunt, Shannon D.; Yatham, Padmaja; Stiles, James; , "Intrapulse Radar-Embedded Communications," *Aerospace and Electronic Systems, IEEE Transactions on* , vol.46, no.3, pp.1185-1200, July 2010.

[58] D. Wilde, *Optimum Seeking Methods*. Englewood Cliffs, NJ: Prentice-Hall, 1964.

[59] Baylis, C.; Lardizabal, S.; Dunleavy, L.; , "A Fast Sequential Load-Pull Algorithm Implemented to Find Maximum Output Power," *Wireless and Microwave Technology Conference, 2006. WAMICON '06. IEEE Annual* , vol., no., pp.1-4, 4-5 Dec. 2006.

[60] C. Baylis, J. Martin, M. Moldovan, O. Akinbule, and R.J. Marks II, "A Test Platform for Real-Time Waveform and Impedance Optimization in Microwave Radar Systems," International Waveform Diversity and Design Conference, Kauai, Hawaii, January 2012.

[61] C. Baylis, “Improved techniques for nonlinear electrothermal FET modeling and measurement validation,” Ph.D. dissertation,Univ. South Florida, 2007.

[62] Agilent Technologies, “Circuit Envelope Simulation”, chp.1, pp. 10-21, 2004.

[63] Jakabosky, J.; Blunt, S.D.; Cook, M.R.; Stiles, J.; Seguin, S.A.; , "Transmitter-in-the-loop optimization of physical radar emissions," *Radar Conference (RADAR), 2012 IEEE* , vol., no., pp.0874-0879, 7-11 May 2012.